

The Black Hole-Bulge Relationship in Luminous Broad-Line Active Galactic Nuclei and Host Galaxies

Jiajian Shen

Daniel E. Vanden Berk

Donald P. Schneider

Department of Astronomy and Astrophysics, The Pennsylvania State University,
University Park, PA 16802

and

Patrick B. Hall

Department of Physics and Astronomy, York University, 4700 Keele St.,
Toronto, ON, M3J 1P3, Canada

ABSTRACT

We have measured the stellar velocity dispersions (σ_*) and estimated the central black hole (BH) masses for over 900 broad-line active galactic nuclei (AGNs) observed with the Sloan Digital Sky Survey. The sample includes objects which have redshifts up to $z = 0.452$, high quality spectra, and host galaxy spectra dominated by an early-type (bulge) component. The AGN and host galaxy spectral components were decomposed using an eigenspectrum technique. The BH masses (M_{BH}) were estimated from the AGN broad-line widths, and the velocity dispersions were measured from the stellar absorption spectra of the host galaxies. The range of black hole masses covered by the sample is approximately $10^6 < M_{\text{BH}} < 10^9 M_\odot$. The host galaxy luminosity-velocity dispersion relationship follows the well-known Faber-Jackson relation for early-type galaxies, with a power-law slope 4.33 ± 0.21 . The estimated BH masses are correlated with both the host luminosities (L_H) and the stellar velocity dispersions (σ_*), similar to the relationships found for low-redshift, bulge-dominated galaxies. The intrinsic scatter in the correlations are large (~ 0.4 dex), but the very large sample size allows tight constraints to be placed on the mean relationships: $M_{\text{BH}} \propto L_H^{0.73 \pm 0.05}$ and $M_{\text{BH}} \propto \sigma_*^{3.34 \pm 0.24}$. The amplitude of the $M_{\text{BH}} - \sigma_*$ relation depends on the estimated Eddington ratio, such that objects with larger Eddington ratios have smaller black hole masses than expected at a given velocity dispersion. While this

dependence is probably caused at least in part by sample selection effects, it can account for the intrinsic scatter in the $M_{\text{BH}} - \sigma_*$ relation, and may tie together the accretion rate with physical properties of the host bulge component. We find no significant evolution in the $M_{\text{BH}} - \sigma_*$ relation with redshift, up to $z \approx 0.4$, after controlling for possible dependencies on other variables. Interested readers can contact the authors to obtain the eigenspectrum decomposition coefficients of our objects.

Subject headings: galaxies: active — galaxies: bulges — galaxies: nuclei — quasars: general

1. Introduction

It is now widely accepted that all galaxies with a massive bulge component contain a central massive black hole (BH). Application of stellar dynamical and gas dynamical techniques for measuring masses of central BHs in normal galaxies has led to the identification of correlations between the BHs and host galaxies (Kormendy & Richstone 1995; Magorrian et al. 1998). The tightest of these relationships are the correlations of BH mass (M_{BH}) with the galaxy bulge luminosity and the bulge stellar velocity dispersion (σ_*) (Ferrarese & Merritt 2000; Gebhardt et al. 2000a; Tremaine et al. 2002).

Massive BHs have also been postulated in quasars and active galaxies (Lynden-bell 1969; Rees 1984). The question of whether AGNs follow a similar BH-bulge relation as normal galaxies is a very interesting one, since it may elucidate the connection between the host galaxy and the active nucleus. Comparisons between the bulge and BH properties in quasars and bright Seyfert galaxies is observationally very difficult, however, since the stellar component near the BH is easily lost in the glare of the active nucleus.

Reverberation mapping (e.g. Blandford & McKee 1982; Peterson 1993; Netzer & Peterson 1997; Peterson et al. 2004 and references therein) of the broad emission lines in AGNs has been used to determine the size of the broad line region (BLR), $R_{\text{BLR}} = c\tau$, where τ is the time lag between continuum and emission line variations. Assuming that the widths of permitted emission lines (e.g., $\text{H}\beta$) are due to virialized gas motions in the BH potential, the BH mass can be estimated from the velocity dispersion ΔV and the radius at the location of the gas R_{BLR} . The central BH mass is then given by

$$M_{\text{BH}} = f \frac{R_{\text{BLR}} \Delta V^2}{G}, \quad (1)$$

where f is a factor of order unity that depends on the structure and geometry of the BLR.

Multiple line observations show an anticorrelation between emission-line lags and line widths, i.e., $\tau \propto \Delta V^{-2}$ (Peterson & Wandel 1999, 2000; Onken & Peterson 2002; Kollatschny 2003), which strongly supports the interpretation that the BLR dynamics are dominated by the BH gravitational potential. Thus, reverberation mapping provides an important technique for estimating the central BH masses of AGNs. The most complete reverberation-based BH masses can be found in Peterson et al. (2004). Another important result of reverberation mapping is the discovery of a simple power law relationship between the continuum luminosity and the size of BLR, $R_{BLR} \propto L^\alpha$ (Kaspi et al. 2000, 2005; Bentz et al. 2006). The value of α using optical wavelengths and the broad Balmer emission lines, and after correcting for the contribution of host galaxy light, is found to be ≈ 0.5 , which is consistent with simple photoionization expectations (Bentz et al. 2006). The radius-luminosity relationship provides a secondary method of estimating the BH masses, suitable for use with single-epoch spectra. The single-epoch spectra technique has been applied to large samples of broad line AGNs to estimate BH masses (Vestergaard 2002; McLure & Jarvis 2002; Netzer 2003; Warner et al. 2003; Wu et al. 2004; Vestergaard 2004; Vestergaard & Peterson 2006).

The difficulty of measuring the host bulge properties remains, however. Image decomposition techniques can separate the host from the central AGNs in some cases (e.g. McLure et al. 2000; Peng et al. 2002; Kulbrodt et al. 2004; Bentz et al. 2006), but they do not provide the necessary spectroscopic information, such as the stellar absorption lines that are necessary for measuring host galaxy stellar velocity dispersions (σ_*). Host galaxy stellar velocity dispersions have been directly measured in some cases by fitting the stellar absorption lines of the Ca II triplet at a wavelength of $\lambda \approx 8550 \text{ \AA}$ (e.g. Ferrarese et al. 2001; Barth et al. 2002; Nelson et al. 2004; Onken et al. 2004; Greene & Ho 2006b). However, the Ca II triplet is difficult to observe for large samples of AGNs, for the following three reasons. First, the lines are often redshifted out of the observable spectral range. Second, the lines are usually contaminated by night sky emission and absorption features. Finally, the host galaxy is usually very faint as compared to the active nucleus, causing the absorption lines to be very weak in contrast to the nuclear continuum. When the Ca II triplet is not available, the [O III] $\lambda 5007$ narrow emission line is sometimes used as a surrogate for estimating the stellar velocity dispersion (Nelson 2000; Shields et al. 2003; Grupe & Mathur 2004; Salviander et al. 2006). However, while there is a correlation between the width of [O III] and σ_* measured from absorption lines, the scatter in the relationship is substantial (Nelson & Whittle 1996; Onken et al. 2004; Botte et al. 2005; Woo et al. 2006). So while the width of [O III] may be used as a surrogate for σ_* in a statistical sense, the BH mass estimated from [O III] can be uncertain by a factor of 5 (Nelson 2000; Boroson 2003; Bonning et al. 2005; Boroson 2005). Thus, the published measurements of host galaxy velocity dispersions for Seyfert 1 galaxies and quasars are few in number (< 100), which prevent statistically

significant investigations of the $M_{\text{BH}}\text{-}\sigma_*$ relationship.

Principal component analysis (PCA) has been performed on both galaxy (Yip et al. 2004a) and quasar (Yip et al. 2004b) samples from the Sloan Digital Sky Survey (SDSS; York et al. 2000). These studies have shown that galaxies and quasars can be classified based on only a few eigencoefficients in each case. The galaxy spectroscopic sample variance is strongly concentrated in just the first few eigenspectra, with over 98% of the information contained in the first three eigenspectra (Yip et al. 2004a). The quasar information is not as strongly concentrated as in the case of galaxies, but the first 10 quasar eigenspectra account for $\approx 92\%$ of the sample variance (Yip et al. 2004b). At low luminosities, the quasar second eigenspectrum has a strong galactic component that resembles the first galaxy eigenspectrum. Vanden Berk et al. (2006, hereafter VB06) used separate sets of galaxy and quasar eigenspectra to efficiently and reliably separate the AGNs and host spectroscopic components. Their tests showed that the technique accurately reproduces the host galaxy spectrum, its contributing flux fraction, and its classification. Inspired by the success of the spectral decomposition, we have separated the host galaxies from the broad line AGNs in a large sample of spectra using the technique of VB06. Among the merits of this method is that a large sample of host galaxy spectra is available from which the stellar velocity dispersions can be measured by the stellar absorption lines. Another advantage of this method is that the BH masses are more accurately measured by using the host-subtracted AGNs than by using composite spectra, especially when host galaxy contributions are not negligible (Bentz et al. 2006). The purpose of this work is to study the BH-bulge relationships for active galaxies in a more statistically meaningful way, given that we can obtain both host and AGN properties for a large number of objects.

The structure of this paper is as follows. In §2 we describe our sample selection, and in §3 we describe the data analysis. The main results of the AGN and host parameter correlations are included in §4. A discussion and summary follow in §5. Throughout the paper we assume a cosmology consistent with recent results from the WMAP experiment (Spergel et al. 2006): $\Omega_m=0.3$, $\Omega_\Lambda = 0.7$ and $H_0 = 70 \text{ km s}^{-1} \text{ Mpc}^{-1}$.

2. Observations and Sample definition

The broad-line AGNs used for this study were selected from the SDSS. The SDSS is a project to image approximately 10^4 deg^2 of sky, in five broad photometric bands (u, g, r, i, z) to a depth of $r \sim 23$, and to obtain spectra of 10^6 galaxies and 10^5 quasars selected from the imaging survey (Fukugita et al. 1996; Hogg et al. 2001; Ivezić et al. 2002; Smith et al. 2002; Pier et al. 2003). Imaging observations are made with a dedicated 2.5 m telescope

(Gunn et al. 2006), using a large mosaic CCD camera (Gunn et al. 1998) in a drift-scanning mode. The SDSS spectra are obtained using a pair of multi-object spectrographs that simultaneously accept 320 optical fibers each (see Stoughton et al. 2002; Blanton et al. 2003). Each fiber subtends a $3''$ diameter on the sky (see § 3.6 for a discussion of fiber size effects). The wavelength range of each spectrum is approximately 3800-9200Å, with a resolution of $\lambda/\Delta\lambda \approx 1850$. The total spectral integration time is at least 45 minutes.

We define broad-line AGNs here to mean any extragalactic object with at least one spectroscopic emission line with a FWHM of at least 1000 km s^{-1} , regardless of the object luminosity or morphology. Broad-line AGN candidates are selected from SDSS color space, or as unresolved matches to sources in the FIRST radio catalog (Becker, White, & Helfand 1995), as described by Richards et al. (2002). Quasars are also often identified because the objects were targeted for spectroscopy by non-quasar selection algorithms, such as optical matches to ROSAT sources (Stoughton et al. 2002; Anderson et al. 2003), various classes of stars (Stoughton et al. 2002), so-called serendipity objects (Stoughton et al. 2002), and galaxies (Strauss et al. 2002). The completeness of the SDSS quasar selection algorithm is close to 95% up to the i band limiting survey magnitude of 19.1 (Vanden Berk et al. 2005).

The set of AGNs studied here were selected from the list given by VB06. In that study, the AGNs were drawn from the catalog of SDSS Data Release Three quasars described by Schneider et al. (2005), and from an extension to that catalog that was constructed by including objects with absolute magnitudes fainter than $M_i = -22$, which is the limit imposed by Schneider et al. (2005). From that sample, VB06 selected 4666 AGNs for which a host galaxy spectral component could be reliably decomposed, using their eigenspectrum technique. Those AGNs have redshifts of $z < 0.752$, and host galaxy fractional flux contributions, F_H , of greater than 10% between 4160 and 4210Å. The selected spectra were corrected for foreground Galactic extinction using the Milky Way extinction curve described by Fitzpatrick (1999), and the reddening maps provided by Schlegel et al. (1998). The decomposition technique uses separate sets of five galaxy eigenspectra and ten quasar eigenspectra to efficiently and reliably separate the AGN and host spectroscopic components. The technique accurately reproduces the host galaxy spectrum, its contributing fraction, and its classification. The details of the AGN and host galaxy decomposition are given by VB06, along with the decomposition parameters and various derived parameters for each object. For clarity, throughout this paper we define the original spectra before decomposition as the active galaxy spectra, the host galaxy components reconstructed with galaxy eigenspectra as the *reconstructed* host galaxy spectra, and the AGN spectra reconstructed with quasar eigenspectra as the *reconstructed* AGN spectra.

For the current study we made additional restrictions on the initial set of 4666 AGNs.

Each of the decomposed components (AGN and host galaxy) must have a sufficiently high signal-to-noise ratio (S/N) to reliably estimate the black hole masses and stellar velocity dispersions, respectively. Because the $M_{\text{BH}} - \sigma_*$ relation applies only to the bulge component of the host galaxies, we also required that the *reconstructed* host galaxy components be dominated by bulge or “early-type” spectra. Quantitatively, the following criteria were applied: 1) The host flux fraction F_H , must be between 0.2 and 0.8, which guarantees that the AGN and host galaxy are both significant contributors to the active galaxy spectrum. 2) The host galaxy classification angle ϕ_H , defined using the values of the first two eigencoefficients (see VB06 and Yip et al. (2004a)), must be in the range $0^\circ < \phi_H < 15^\circ$, which selects bulge-dominated galaxy spectra. The spectrum classification is based on the flux within SDSS fiber apertures ($3''$). For a galaxy dominated by a bulge component in the SDSS spectrum, the morphology of the entire galaxy image, extending beyond the $3''$ aperture, may or may not be classified as early type. Thus, this criterion does not guarantee that the host galaxy would be classified *morphologically* as a bulge-dominated galaxy. However, this spectroscopic study focuses on the bulge component of the galaxies, regardless of the extended morphology. Within the $3''$ fiber aperture, the selected sample galaxies are all bulge dominated. 3) The active galaxy spectrum must have a mean S/N per pixel > 15 , averaged over the SDSS i band sensitivity function. We also required the redshifted position of the $H\beta$ line to be covered by the spectra, but that constraint was already satisfied by the $z < 0.752$ limit in the VB06 sample. In practice the S/N requirement limited the maximum redshift to be far below 0.75. These criteria resulted in a sample of 960 spectra, with redshifts from 0.013 to 0.489 (the median redshift is 0.153) and S/N from 15.0 to 65.7 (the median S/N is 21.6). Figure 1 shows the relation between the i band S/N and the apparent magnitude m_i . Figure 2 shows the S/N level as a function of redshift. Figure 3 shows the AGN component luminosity L_{5100} (the monochromatic continuum luminosity at a rest wavelength of 5100\AA (see § 3.2)), as a function of redshift for the sample. The correlation of luminosity with redshift is due mainly to the apparent magnitude limit imposed by the SDSS quasar selection algorithm.

It is possible that some low redshift, extraordinarily luminous objects are missed because of the SDSS upper flux limits ($i = 15$). However, these should be relatively rare objects since the SDSS completeness to broad-line AGN is extremely high, $\sim 95\%$ (Vanden Berk et al. 2005). Moreover, since the relative brightness of the AGN and host is one of our selection criteria ($0.2 < F_H < 0.8$), these most luminous objects would not be selected for our sample since the flux is dominated by nuclear light. At the other extreme, the sample certainly omits the least luminous nuclear sources, both because of the SDSS faint flux limits, and because host galaxy light would dominate the flux. These objects would presumably, though not certainly, have properties that lie somewhere between those of the relatively brighter objects in our sample, and the galaxies with quiescent supermassive black holes examined

in other studies (e.g. Tremaine et al. 2002).

3. Data Analysis

3.1. Estimation of Black Hole Mass

The BH masses were estimated by equation (1), which requires the widths of the broad emission lines ΔV or FWHM, the distance of the broad emission line gas from the central gravitational source R_{BLR} , and the scale factor f . The broad emission line widths can be measured directly from the spectra. The gas radius cannot be measured directly from single-epoch spectra, so we use the result based on reverberation mapping studies that the continuum luminosity and radius are strongly correlated. The radius-luminosity (R-L) relationship has been calibrated using the gas distances from samples of objects for which reverberation mapping techniques could be used. The power-law index for the correlation between gas radius and the optical luminosity at 5100Å, L_{5100} , was reported to be about 0.67-0.70 by Kaspi et al. (2000, 2005). However, the R-L relationship can be affected by host galaxy contamination; using new *Hubble Space Telescope* (*HST*) imaging of reverberation-mapped AGNs, Bentz et al. (2006) corrected the host galaxy contamination of the optical continuum luminosity and reported a flatter power-law index of 0.52. Since our study deals with the nuclear luminosities, separated from the host stellar contribution, we adopted the R-L relationship from Bentz et al. (2006). The value of the scale factor f is unknown. However, using the reanalyzed reverberation mapping BH masses of Peterson et al. (2004) and *assuming* that the active galaxies obey the same $M_{\text{BH}} - \sigma_*$ relationship as quiescent galaxies (Tremaine et al. 2002), Onken et al. (2004) derived a value for f by requiring the two techniques yield statistically consistent BH masses. In this paper we use the most recently determined mass scaling relationship from Vestergaard & Peterson (2006), which was calibrated by combining the R-L relationship by Bentz et al. (2006) and the scale factor by Onken et al. (2004). The mass scaling relationship for single epoch spectra, using the FWHM of the broad H β emission line, and the monochromatic continuum luminosity at 5100Å, L_{5100} , is given as (Vestergaard & Peterson 2006)

$$\log M_{\text{BH}} = \log \left\{ \left(\frac{\text{FWHM}_{\text{H}\beta}}{10^3 \text{ km s}^{-1}} \right)^2 \left(\frac{\lambda L_{5100}}{10^{44} \text{ ergs}} \right)^{0.5} \right\} + (6.91 \pm 0.02), \quad (2)$$

where M_{BH} is the BH mass in solar units. The zero point error in equation (2) is a formal statistical error. A more representative uncertainty in the zero point for an individual object is the intrinsic scatter about the relationship of ± 0.43 dex. The measurements of the H β FWHM and L_{5100} for our sample of AGNs are described in the following subsections.

3.2. Emission Line Width Measurement

The 960 spectra were first decomposed into host galaxy and AGN spectra using the eigenspectrum method described by VB06. Examples of the spectroscopic decomposition of the objects with different S/N are shown in Figs. 4, 5, and 6. One can also refer to Fig. 9 in VB06 for more decomposition examples. In each of the examples, the original spectrum is shown along with the *reconstructed* AGN and host galaxy spectra and the fit residuals. The *reconstructed* spectrum is a close match to the original active galaxy spectrum, except for some larger residuals in the regions of narrow and broad emission lines. Accurately reconstructing the emission lines can require a large number of eigenspectra, which may introduce spurious features into the reconstructed continuum (VB06).

To measure the AGN emission lines, we do not use the *reconstructed* AGN spectrum, but instead use the original active galaxy spectrum with the *reconstructed* host spectrum subtracted. Because we do not use the *reconstructed* AGN spectrum for our analysis of the emission lines, the imperfect modeling of the AGN broad lines as seen in the residuals in Fig. 4 does not affect the FWHM measurements of the broad lines. In subtracting the host spectrum, we are very careful in dealing with the narrow lines. After decomposing an active galaxy spectrum, the *reconstructed* host galaxy spectrum is interpolated across the narrow line regions, effectively removing the narrow lines. The interpolated *reconstructed* host spectrum is then subtracted from the original active galaxy spectrum. The resulting AGN spectrum thus contains both the host and AGN components of the narrow line regions. This method is better at preserving the details of the AGN broad emission line profile, and it retains the noise of the original spectrum, which is necessary to assess the quality of the spectral measurements. We define the host-subtracted active galaxy spectrum as the *decomposed* AGN spectrum. The *decomposed* AGN spectrum should be differentiated from the *reconstructed* AGN spectrum. As mentioned above, the *decomposed* AGN spectrum has had the host spectrum subtracted, and it retains all of the necessary original spectrum information, such as emission lines and noise. However, the *reconstructed* AGN spectrum is reconstructed by the eigenspectra and the eigencoefficients — this spectrum is not used for any spectroscopic measurements. Figs. 7, 8, and 9 show examples of *decomposed* AGN spectra, which clearly show that the emission lines are preserved, even in the narrow line regions. The monochromatic luminosities at 5100\AA of the sample objects were measured from the rest frame *decomposed* AGN spectra, by averaging over a 10.57\AA (10-pixel) wide region centered on 5100\AA .

The $H\beta$ profile is not always sufficiently strong in our spectra to accurately determine its FWHM. We also measured the FWHM of $H\alpha$ for all objects possible because, as shown by Greene & Ho (2005), one can use the $H\alpha$ line width to approximate the width of the

H β line when the latter is unavailable. This issue and the results are discussed further in § 3.3. The widths of the emission lines were determined by fits to the line profiles in the regions near each of the lines. To fit the H α and H β lines, a featureless power-law continuum and Fe II template were first fit to the *decomposed* AGN spectrum. The H α and H β lines were fitted separately. We adopted a local power law to fit the underlying continuum; the ostensibly line-free continuum end points were selected as 4270Å and 5600Å for H β lines, and as 6270Å and 6980Å for H α lines. The average fluxes of the end points, averaged over the 21 pixel wide regions centered on the end points, were used to fit the power law continuum. Following Boroson & Green (1992), an effective Fe II template can be generated by simply broadening and scaling the Fe II spectrum derived from observations of the narrow line Seyfert 1 galaxy I Zw 1 (kindly provided by T. Boroson). Although a newer template is available (Véron-Cetty et al. 2004), we still use the template of Boroson & Green (1992) because one of our aims is to compare our results to those of previous studies, all of which used the Boroson & Green (1992) template. The Fe II template strength is free to vary, but it is broadened to be consistent with the FWHM of H β for each object (Boroson & Green 1992; Shang et al. 2005). In order to avoid contamination from strong spectral lines, we include only the following regions in the Fe II fit: 4450-4750Å and 5100-5350Å (Greene & Ho 2005). The best Fe II template is found by the minimization of the χ^2 values in the fit region. The Fe II template is very weak and may be negligible in the local region of the H α line. Examples of continua and Fe II template fits to *decomposed* AGN spectra in our sample are shown in Figs. 7, 8, and 9.

After subtracting the continuum and iron template, the remaining broad and narrow emission features near H β and H α were fit with a series of Gaussian profiles. The broad component of the H β line was fit with two Gaussians, which are usually sufficient to account for the width and possible asymmetry of the line (Shang et al. 2005). Each of the [O III] $\lambda\lambda$ 4959, 5007Å lines and the narrow component of the H β line were fit by single Gaussians. The broad component of the H α line was also fit by two Gaussians, and a single Gaussian was used for each of the [N II] $\lambda\lambda$ 6548, 6583Å lines and the narrow component of the H α line. The relative positions of the narrow H α and [N II] lines were constrained by their laboratory values, and the relative ratio of the two [N II] components was fixed to 2.96. For the H β line fits, however, we did not set as many strict constraints as we did for H α . Instead, we allow a few Å shift for each line position, and let the peaks of the [O III] doublet lines vary independently. The H β constraints are looser than those for H α because H β is weaker than H α . For example, if many restrictions are placed on the fit to the [O III] doublets, the fit to the broad H β line can become unreliable in some cases. Although the peaks and fluxes of the [O III] doublet lines were allowed to vary independently, the doublet flux ratios in our sample (Fig. 10) are close to the theoretical value of 3:1. All of the Gaussian components

within either the $H\beta$ or $H\alpha$ set were fit simultaneously, with the narrow-line dispersions all constrained to be smaller than 5\AA (308.6 km s^{-1}). The best-fit parameters were determined through a minimization of the χ^2 statistic, using the non-linear Levenberg-Marquardt minimization algorithm as implemented by *mpfit* in IDL¹. Using the fitted model profiles and excluding the narrow components, we calculated the final FWHM of the $H\beta$ and $H\alpha$ lines based on an analytic solution from the sum of the two fitted broad Gaussian components. The SDSS spectrograph wavelength dispersion (160 km s^{-1}) does not increase the broad emission line widths by any more than 1% even in the worst case. Example fits to the $H\beta$ and $H\alpha$ line regions are shown in Fig. 11, which shows the *decomposed* AGN spectrum, the fit, the narrow and broad components of the fit, and the fit residuals.

To estimate the errors in the line width measurements, we used a method similar to that of Greene & Ho (2005). An artificial spectrum was generated for each object by combining the best-fit model emission lines with Gaussian random errors according to the object’s error array. Then the artificial spectra were fit using our fitting procedure, as outlined above. Each spectrum was simulated by 100 realizations (a larger number of realizations did not significantly improve the error estimation), and the estimated error was simply taken to be the dispersion in the 100 measurements. The error measured in this way is the formal error, which accounts only for the random noise error in the FWHM measurement. Additional uncertainties come from the uncertainty of the fitted local continuum, and imperfect removal of the Fe II components. Assuming a single Gaussian profile, if the continuum is lowered by 10% of the line peak, the estimated FWHM will increase by 7%. If we do not remove the Fe II components at all, the typical measured FWHM changes by about 2%.

3.3. The Relationship Between the FWHM of $H\alpha$ and $H\beta$

Inspection of the $H\beta$ region of the spectra showed that some of the broad $H\beta$ lines are either missing (e.g. due to problems with that part of spectrum) or are not detectable in the spectra. In contrast, when $H\alpha$ is in the observable spectral range ($z < 0.36$), the broad component is almost always easily detectable. The $H\alpha$ line can be used to estimate the width of the $H\beta$ line in cases where the $H\beta$ line cannot be measured. We used the $H\beta$ line to estimate M_{BH} when the S/N of the peak of its broad component in the *decomposed* AGN spectrum is at least 3. That criterion is satisfied in 640 of the 960 objects in the full sample. Among the 960 objects, the $H\alpha$ line is not measurable due to bad pixels in 11 cases and because it is redshifted outside of the observed wavelength range in 17 cases. In

¹IDL is a trademark of Research Systems, Inc.

38 cases, the FWHM of the $H\alpha$ line is smaller than 25\AA (1143 km s^{-1}), so that the narrow and broad components could not be unambiguously separated; these spectra were excluded from further $H\alpha$ analysis. In eight cases, the profiles of the $H\alpha$ and $H\beta$ lines possess double emission profiles and extremely broad wings, making the meaning of FWHM ambiguous in these cases; these spectra were also excluded from further analysis. In total, there are 886 spectra for which the $H\alpha$ line width was reliably measured.

Among the 640 good $H\beta$ and 886 good $H\alpha$ spectra, there are 597 spectra for which the widths of both lines can be measured. The FWHM of $H\alpha$ and $H\beta$ for these spectra are plotted in Fig. 12; it is clear that there is a relatively tight relationship between the two line widths, $\text{FWHM}_{H\alpha}$ and $\text{FWHM}_{H\beta}$. When fitting the relationship, neither $\text{FWHM}_{H\alpha}$ nor $\text{FWHM}_{H\beta}$ can be regarded as the independent variable, so we calculate the best fit line to the logarithmic quantities using the “BCES” (Bivariate Correlated Error and intrinsic Scatter) bisector estimator described by Akritas & Bershady (1996), which takes uncertainties in both parameters into account. The best fit relationship using the BCES bisector estimator is

$$\frac{\text{FWHM}_{H\beta}}{10^3 \text{ km s}^{-1}} = (1.16 \pm 0.02) \times \left(\frac{\text{FWHM}_{H\alpha}}{10^3 \text{ km s}^{-1}} \right)^{0.99 \pm 0.02} \text{ km s}^{-1} \quad (3)$$

This result is similar to that found by Greene & Ho (2005), and the scatter of equation (3) is about 0.06dex ($\sim 470 \text{ km s}^{-1}$). In Fig. 12, the solid line shows the best fit, and the dashed line denotes $\text{FWHM}_{H\alpha} = \text{FWHM}_{H\beta}$. The filled dots are the mean spectrum FWHM from Kaspi et al. (2000) for comparison; those points are also described well by the best fit relation.

3.4. Uncertainty in BH Mass Estimates

The uncertainties of the FWHM measurements for $H\alpha$ and $H\beta$ and of the continuum luminosity include not only the errors from the fitting routine, but also the errors that arise in the decomposition of the AGN spectrum from the original active galaxy spectrum. We estimated the total uncertainty by using simulations in the following way. For a typical object with the median S/N of the sample, we simulated 100 spectra by adding random noise to the original active galaxy spectrum according to its error array. Each of the 100 simulated spectra was decomposed, and the continuum luminosity and FWHM of the emission lines were fit as described above.

The uncertainty in each parameter was calculated by measuring the rms dispersion of the 100 measurements. The typical rms dispersions for the FWHM measurement of $H\alpha$ and $H\beta$ are 4% and 7% respectively; the luminosity at 5100\AA has a typical dispersion of

4%. The final uncertainty for the BH mass by equation (2) is 7% and 14% respectively, using the FWHM of $H\alpha$ and $H\beta$. A representative value of the uncertainty in the BH mass for an individual object is the zero point uncertainty of the mass scaling relationship, e.g. equation (2). The standard deviation of the zero point (intrinsic scatter) is $\pm 0.43\text{dex}$ (Vestergaard & Peterson 2006).

Figure 13 shows the distribution of the AGN monochromatic continuum luminosity, L_{5100} . The solid line is the distribution of L_{5100} after subtracting the host galaxy component. The dotted line shows the estimated L_{5100} values when the host galaxy component is not subtracted; these values were estimated directly from the extinction corrected active galaxy spectrum at rest-frame 5100\AA , averaged over a 10-pixel wide region. It is clear that the host galaxy component is non-negligible in our sample; the difference between the luminosity with and without host galaxy subtraction is close to 0.5 dex. This implies that the host galaxy components can significantly affect the accuracy of the BH mass estimates at the luminosities present in our sample. The host galaxy contribution will also affect the luminosity-radius relationship, as discussed by Bentz et al. (2006).

3.5. BH Mass Distribution

The black hole masses were calculated according to equation (2). The FWHM of the $H\beta$ line was used directly in the 640 cases for which the line could be measured. For the 286 cases in which the $H\alpha$ line was measurable when $H\beta$ was not, the $H\alpha$ FWHM was used to estimate the FWHM of the $H\beta$ line according to equation (3). The distribution of black hole masses is shown by the dotted histogram in Fig. 14. Most of the black hole masses are in the range $10^6 < M_{\text{BH}} < 10^9 M_{\odot}$. From the black hole masses and the continuum luminosities, we can estimate the Eddington ratio, $L_{\text{bol}}/L_{\text{Edd}}$ — the ratio of the AGN bolometric luminosity to the Eddington luminosity for the black hole — using the approximate relation $L_{\text{bol}} \approx 10\lambda L_{\lambda}(5100\text{\AA})$ (e.g., Wandel et al. 1999). The estimated Eddington ratio has a standard deviation of 25% due to variations in the bolometric correction (Richards et al. 2006). Since L_{Edd} is proportional to M_{BH} , the Eddington ratio would have a standard deviation of $\approx 28\%$, assuming the typical error in our BH mass estimates (§3.4). The solid histogram in Fig. 14 shows the distribution of $L_{\text{bol}}/L_{\text{Edd}}$; the Eddington ratios also fall within a limited range, mostly at small values. The small Eddington ratios and limited range of BH masses are due to the sample selection criteria, which require that the stellar absorption features are detectable at a level that allows the host galaxy velocity dispersions to be measured.

Fig. 15 shows the relationship between BH mass and the estimated Eddington ratio $L_{\text{bol}}/L_{\text{Edd}}$. In our data sample the BH mass is inversely correlated with the Eddington ratio.

This is not unexpected if the range of bolometric luminosities does not change proportionally with M_{BH} . Both M_{BH} and $L_{\text{bol}}/L_{\text{Edd}}$ are parameters calculated from AGN continuum luminosity $L_{\text{AGN}} \approx \lambda L_{\lambda}(5100 \text{ \AA})$, and emission line FWHM. Therefore, Fig. 15 is simply a remapping of the sample L_{AGN} and FWHM values. The correlation is due in part to sample selection effects in the SDSS and our sample. Since our sample is selected only from SDSS AGN with detectable stellar features ($0.2 < F_H < 0.8$), the luminosity cannot be above the SDSS bright limit for spectroscopy ($i = 15$). Our sample is neither so bright that the flux is dominated by nuclear light, nor so faint that the flux is dominated by host galaxy light. Thus, objects with higher BH masses tend to have a lower range of Eddington ratios, and vice versa. The dispersion in the relationship is largely due to the range of measured emission line widths that are used to calculate M_{BH} .

3.6. Host Galaxy Velocity Dispersion Measurement

Two accurate and objective methods, the *Fourier-fitting* method and the *direct-fitting* method, have been developed for measuring the stellar velocity dispersion (Sargent et al. 1977; Tonry & Davis 1979; Franx et al. 1989; Bender 1990; Rix & White 1992; Barth et al. 2002; Greene & Ho 2006b). They are all based on a comparison between broadened template spectra and the spectrum of the galaxy whose velocity dispersion is to be determined. Fourier space is the natural choice to estimate the velocity dispersions because a galaxy’s spectrum is a mix of stellar spectra convolved with the distribution of velocities within the galaxy. However, there are several advantages to treating the problem entirely in pixel space, rather than Fourier space. Specifically, the effects of noise are much more easily incorporated in the pixel-space-based direct-fitting method. We have used the “direct-fitting” method (e.g. Rix & White 1992; Bernardi et al. 2003a), in which the spectrum is directly fit in pixel space. We use the public IDL program *vdspfit*, written by David Schlegel, to find the velocity dispersions for the host galaxies. The templates consist of the first four eigenspectra from a principal component analysis of the echelle stellar spectra in the Elodie database (Moultaka et al. 2004). The best-fitting dispersion value was determined by minimizing χ^2 for the fit.

The *reconstructed* host galaxy spectrum was not used to measure the velocity dispersion, because features such as narrow absorption line profiles may not be well reconstructed without invoking a much larger number of galaxy eigenspectra than we have used here. Instead, we used the observed active galaxy spectrum after subtracting the *reconstructed* AGN component, which we define as the *decomposed* host galaxy spectrum. This method allows us to use the error array of the original spectrum to determine measurement uncertainties.

In the fitting routine, all of the narrow *emission* lines were blocked, because there is very little information about the absorption spectrum in those regions, and the AGN fit to the narrow emission lines may be poor. We also blocked the broad emission line regions of $H\alpha$ and $H\beta$ to avoid any artifacts introduced by imperfectly *reconstructed* AGN components.

An example fit of a host galaxy (from among the same objects used as examples in Fig. 4), resulting in a measurement of the velocity dispersion, is shown in Fig. 16. In the figure, the two large boxes show the masked broad $H\alpha$ and $H\beta$ line regions; the left and the right small boxes show the masked narrow emission line regions ($H\gamma$ and $[O\text{ I}]$), and the middle small box shows the masked bad pixel region.

The SDSS spectra were obtained by using a fixed $3''$ fiber, which covers different fractions of the projected areas of different objects, due both to different intrinsic galaxy sizes and different redshifts. Thus, the velocity dispersions should not be compared without accounting for the finite fiber diameter, which is discussed here. The dispersion is scaled to a standard relative circular aperture, defined to be one-eighth of the effective galaxy radius. The correction formula was applied following Jørgensen et al. (1995) and Wegner et al. (1999)

$$\frac{\sigma_{\text{cor}}}{\sigma_{\text{est}}} = \left(\frac{r_{\text{fiber}}}{r_0/8} \right)^{0.04}, \quad (4)$$

where $r_{\text{fiber}} = 1''.5$ and r_0 is the effective radius of the galaxy measured in arcseconds. Bernardi et al. (2003a) studied early type galaxies up to a redshift of $z = 0.3$ and showed that most galaxies have $r_0 \geq 1''.5$. Our sample has almost the same redshift limit as that of Bernardi et al. (2003a) and the correction depends only weakly on r_0 , so the correction is not large. The effective radii of the galaxies in our sample have not yet been measured, so we assume that all of the early type galaxies (or the galaxy bulges) in our sample have typical effective radii, which corresponds to an angular size of $r_0 = 1''.5$ at a redshift of $z = 0.3$. At redshifts other than $z = 0.3$, the angular sizes were scaled with distance. The correction has a maximum value of 10.8% and a median value of 5.4%. For a more accurate correction, the effective radii of the hosts must be measured. In the case of inactive galaxies, estimations of effective radii are publicly available parameters measured from SDSS images. For active galaxies, one should first remove the central nucleus to get the host galaxy effective radius, which requires image decomposition to separate the nucleus and host. We have not pursued this additional correction here, owing to the limited improvements possible with SDSS imaging data in relation to the required workload.

3.7. Uncertainty in the Velocity Dispersion Measurement

It was shown by Bernardi et al. (2003a) that the direct-fitting method does not produce large systematic errors, but the same conclusion may not apply to our measurements given the presence of AGN components. Even though a measured velocity dispersion may be accurate for a *decomposed* host galaxy spectrum, it may be different from the true value if the *decomposed* host galaxy is not an accurate representation of the true host galaxy. A test for systematic errors in the velocity dispersion measurement was made by generating simulated data. We first constructed an early type galaxy template using the stellar echelle spectra in the Elodie database. The template early type galaxy has a high S/N and a very small velocity dispersion. The template was broadened with different values of the velocity dispersion, ranging from 60 to 400 km s^{-1} , and rebinned to the same wavelength scale as the SDSS spectra (69 $\text{km s}^{-1}/\text{pixel}$). To each of the broadened galaxy templates, a template AGN spectrum was added to form simulated active galaxy spectra. In all cases, the fractional contribution of the host galaxy was set to $F_H = 50\%$.

The simulated active galaxy spectra were decomposed into host galaxy and AGN components, and the direct-fitting method was used to make measurements of the velocity dispersions. No noise was added to the spectra at this point, so any deviations of the measured velocity dispersions from the true values represent systematic errors in the measurements. Figure 17 (dotted line) shows the relative difference between the true velocity dispersions and the measured values, $\delta\sigma_* = (\sigma_{*,\text{measured}} - \sigma_{*,\text{true}})/\sigma_{*,\text{true}}$. The measured velocity dispersion is systematically approximately 1% smaller than the true velocity dispersion. This systematic error steadily increases to about 4% below velocity dispersions of about 120 km s^{-1} .

To test the effects of noise, we added random noise to the template active galaxy spectra. In our sample, the lowest spectroscopic S/N is 15, which sets the worst case limit in the simulations (of course, objects with a host galaxy fraction of less than the simulation value of $F_H = 50\%$ will usually return poorer results; see below). Random noise corresponding to a S/N of 15 was added to each template 100 times. The noisy spectra were decomposed and the velocity dispersions were measured as usual. The dashed line in Fig. 17 shows the relative error between the true velocity dispersion and the mean measurement in each set of 100 simulated spectra. The solid curves in Fig. 17 show the rms scatter of the velocity measurements from the mean, due to the random error in 100 simulations. Fig. 17 shows that the random error of the velocity dispersion measurement is around 10% for the spectra with the lowest S/N in our sample. The mean relative errors track the noiseless relative errors very closely, showing again an approximately 1% systematic offset. The systematic relative error is larger at smaller velocity dispersions, reaching a maximum absolute value of about 4% at 60 km s^{-1} , which is close to the dispersion per pixel of the SDSS spectrographs

(69 km s⁻¹). Values of the velocity dispersions smaller than this limit are very uncertain.

The *vdispfit* routine returns an estimate of the uncertainty in the velocity dispersion, based on the spectral noise, which we find to be consistent with the results of the simulations. Figure 18 shows the estimated uncertainty in the measurement of the velocity dispersion, returned from the *vdispfit* routine, as a function of the *decomposed* host galaxy S/N . As expected, the errors are generally smaller with increasing S/N . Some of the errors are greater than the worst case results from the simulations, because their host galaxy fractions are less than $F_H = 50\%$. Figure 19 is the simulation of the the worst case ($F_H = 20\%$ and $S/N = 15$), which shows that the maximum error can be 30% for small velocity dispersions. Error may arise if the templates are not good matches to the host galaxy spectra. For example, the templates may not be able to account for a strong post-starburst component. However, all of our host galaxies are chosen so as to be dominated by old stars. In addition, the simulations did not account for bad pixels, night sky line residuals, and other artifacts. The reduced χ^2 values in the velocity dispersion fittings are close to 1, which proves that any template mismatch is negligible in our sample. The vast majority of the objects have velocity dispersion errors of less than 15%.

3.8. The AGN and Host Galaxy Data Set

Spectra whose velocity dispersions are less than 69 km s⁻¹ were excluded from further analysis. After all of the selection criteria were applied, there were 617 objects with reliable H β and 840 with reliable H α line measurements, all of which also have reliable velocity dispersion measurements.

Black hole masses were calculated using the H β FWHM in the 617 cases for which it was measurable, and in another 286 cases, using an estimate of the H β FWHM based on the H α measurements and equation (3). The total number of objects (out of the initial 960) with reliable parameter measurements is 903. The electronic version of Table 1 lists all of the active galaxies and their measured or derived parameters, including redshift, L_{5100} , H α and H β FWHM, M_{BH} , σ_* , and host luminosity (as calculated by VB06). A partial table is shown in the printed version of Table 1.

4. Results

4.1. The fitting algorithm

In the following sections, we will study how the BH masses, host galaxy luminosities and the host velocity dispersions are correlated. We assume that there is an underlying linear relation in the logarithmic quantities for each pair in the form $y = \alpha + \beta x$. The best fit parameters α and β were found by the minimization of χ^2 , defined, following Tremaine et al. (2002), as

$$\chi^2 \equiv \sum_1^N \frac{(y_i - \alpha - \beta x_i)^2}{\epsilon_{yi}^2 + \beta^2 \epsilon_{xi}^2} \quad (5)$$

where x_i, y_i correspond to the measurements for each object, and ϵ_i is the formal uncertainty in the measurement. The 1σ uncertainties in α and β are given by the maximum range of α and β for which $\chi^2 - \chi_{\min}^2 \leq 1$. To minimize χ^2 , we use the Levenberg-Marquardt algorithm as implemented by *mpfit* in IDL, which recovers the results of the Numerical Recipes routine *fitexy* (Press et al. 1992) as implemented in IDL for the case of symmetric errors.

4.2. Host Galaxy Bulge Luminosity and Velocity Dispersion Relation

The luminosities and velocity dispersions of early type galaxies have long been known to be correlated — a phenomenon known as the Faber-Jackson relation (Faber & Jackson 1976). The host galaxy absolute magnitude in the SDSS g band, M_g (calculated by VB06) is shown as a function of velocity dispersion in Fig. 20. The host galaxy M_g range of our sample is very similar to that of the normal elliptical galaxies studied by Bernardi et al. (2003a), except ours are a bit more luminous. There is a wide intrinsic scatter in the Faber-Jackson relation, which we also find in our sample, so for clarity we have binned the values of the host galaxy luminosity in the figure (similar to the procedure used by Bernardi et al. 2003b). Each point represents the average value for at least 50 objects. The bars in the figure show the rms scatter in the velocity dispersion in each bin (the errors on the mean values would be approximately $\sqrt{50}$ times smaller). There is clearly a strong correlation between M_g and σ_* , although we find a slightly larger dispersion about the relation relative to studies of inactive early type galaxies (e.g. Bernardi et al. 2003b), most likely due to the typically smaller S/N in our *decomposed* host spectra. The solid line shows the best power-law fit to the relation

$$L \propto \sigma_*^{4.33 \pm 0.21}, \quad (6)$$

which is consistent with the Faber-Jackson relation for inactive early type galaxies (Bernardi et al. 2003b). Table 2 lists the mean values of the host luminosity, stellar velocity dispersion, black

hole mass, and rms dispersions for the data sets in each bin. The binned values will be used in the analysis of the following subsections.

4.3. Black Hole Mass and Bulge Luminosity Relation

Figure 21 shows the relationship between BH mass and absolute g band magnitude M_g of the host galaxies. Crosses show the mean value in each bin, and error bars show the rms scatter around the mean value. Each point represents the average value for about 50 objects. A linear fit using the logarithmic M_{BH} values gives the relation

$$\log M_{\text{BH}} = -0.29(\pm 0.02)M_g + 1.46(\pm 0.33). \quad (7)$$

From the relation in Eq. 7, we can also derive the expected relationship between M_{BH} and host bulge mass M_{bulge} by assuming that only the host bulge contributes to M_g . We adopt a g -band mass-luminosity relation $M_{\text{bulge}} \propto L_{\text{bulge}}^{1.18 \pm 0.03}$, consistent with the V -band results of Magorrian et al. (1998). Substituting in, we find a relation $M_{\text{BH}} \propto M_{\text{bulge}}^{0.61 \pm 0.05}$. This implies that the $M_{\text{BH}} - M_{\text{bulge}}$ relationship is non-linear in our sample, and it is consistent with the result found by Wandel (2002). However, it is in contrast to the linear relationship found by others (e.g. McLure & Dunlop 2001, 2002). Verification of our result will require more precise measurements of the bulge luminosity, since our measurements rely on spectral decomposition, rather than image decomposition, and we have assumed that the host component of the SDSS g band “cmodel” magnitude contains only the bulge flux. The “cmodel” magnitude uses a best fit linear combination of an exponential and de Vauc. profile, which gives a robust estimate of the total flux from an extended object, regardless of morphology. The bulge flux was estimated by subtracting an appropriately scaled nuclear component flux, derived from the decomposed AGN spectrum, from the “cmodel” magnitude flux, as described by VB06. A more precise bulge luminosity could be obtained from image decomposition, which directly separates out the host galaxy bulge and nuclear AGN components. As a complement to the spectral decomposition, image decomposition is planned for a future paper.

4.4. Black Hole Mass and Velocity Dispersion Relationship

Figure 22 shows the BH mass and σ_* relation for all the individual points, and the dot dashed line is the best fit to the $M_{\text{BH}} - \sigma_*$ relation for inactive galaxies (Tremaine et al. 2002). For $\log \sigma_* > 2.2$, objects in our sample have significantly smaller average BH masses than do inactive galaxies at the same value of σ_* . The measured values of slope β in the $M_{\text{BH}} \propto \sigma_*^\beta$

relation cover a wide range from 3.5 to 5.0 (Ferrarese & Merritt 2000; Gebhardt et al. 2000a). As studied by Tremaine et al. (2002), the wide uncertainties in the slope are due to the use of different statistical algorithms, the unknown intrinsic scatter in the BH mass estimation, and the uncertainties in the velocity dispersions. Our large sample helps reduce some of these uncertainties.

The relationship between the black hole mass and host velocity dispersion was found by averaging the values of the two quantities in bins of host absolute magnitude. That is, the values represented by the points in each M_g bin in Figures 20 and 21 were compared to find the $M_{\text{BH}} - \sigma_*$ relation, which is shown in Fig. 23. The crosses show the mean value in each bin and error bars are the standard deviation of the mean in each bin. Each point represents the mean value for about 50 objects, and the error bars are those in Figures 20 and 21 divided by the square root of the number of objects in each bin. The solid line is the best-fitting linear relation (to the logarithmic quantities)

$$\log M_{\text{BH}} = 3.34(\pm 0.24) \log(\sigma_*/200 \text{ km s}^{-1}) + 7.92(\pm 0.02). \quad (8)$$

The slope found here is 1.7σ flatter than the one found for inactive galaxies by Tremaine et al. (2002), who found a value of 4.02 ± 0.32 . Fixing the slope to that value, the intercept of the best fit to our data becomes 7.96 ± 0.02 , which is smaller than the value of 8.13 ± 0.06 found by Tremaine et al. (2002) by 0.17 dex, a significance of 2.7σ . (In both cases σ is the quadrature sum of the uncertainties of both measurements.) The same $M_{\text{BH}} - \sigma_*$ relation as equation (8) can also be obtained by fitting the individual data points in Figure 22, when an intrinsic scatter of 0.36 dex on BH masses and 0.12 dex on the velocity dispersions are included. This scatter is consistent with the dispersions in each binned data set (see Table 2).

Figure 24 shows the same relationship as Figure 23 but with values from the literature added in the plot. The additional data extends well beyond the dynamic range of our values, particularly toward smaller values of M_{BH} and σ_* . The literature data and uncertainties are all obtained from the table given by Greene & Ho (2006a). The open squares are the data estimated by Greene & Ho (2006a), the asterisks are the data from Onken et al. (2004) and Nelson et al. (2004), and the open triangles are the data from Peterson et al. (2005) and Barth et al. (2004) for NGC 4395 and POX 52 respectively. The filled circles are the binned data from this paper as shown in Fig. 23. In Fig. 24 the solid line is the best fit using all of the data. The dashed line is the fit for inactive galaxies from Tremaine et al. (2002).

The best fit to the $M_{\text{BH}} - \sigma_*$ relation using all of the data is

$$\log M_{\text{BH}} = 3.93(\pm 0.10) \log(\sigma_*/200 \text{ km s}^{-1}) + 7.92(\pm 0.02). \quad (9)$$

This slope is entirely consistent with that measured for inactive galaxies (Tremaine et al.

2002). Fits were also made with a fixed slope of 4.02 to all of the data. The fixed-slope intercept is smaller than the inactive galaxy value of 8.13 by 0.19 dex, a significance of 3σ .

Based on our analysis, we find that the $M_{\text{BH}} - \sigma_*$ relationship for active galaxies in our sample is marginally flatter than that of inactive galaxies, but that it is consistent with that of inactive galaxies if the literature data are added. The flattening is consistent with the study of Greene & Ho (2006a). The intercept of the active galaxy relationship is smaller than that for inactive galaxies. This holds whether or not the literature data are included in the analysis, and is consistent with Nelson et al. (2004) and Greene & Ho (2006a), though with uncertainties ~ 5 times smaller than in the former reference and ~ 2 times smaller than the latter.

We caution that the results presented in this section depended in part on the selection of the mass-scaling relationship used to estimate M_{BH} , and that not all of the literature values were derived using the same relationship that we use here. In particular the intercept of the $M_{\text{BH}} - \sigma_*$ relationship would be even smaller had we used the commonly adopted scale factor value $f = 3$ (which is inconsistent with the value derived empirically by Onken et al. (2004)). The power-law index of the radius-luminosity relationship also affects the slope of the $M_{\text{BH}} - \sigma_*$ relationship. A higher radius-luminosity power-law index (which would be inappropriate for our study since we account for host galaxy flux contamination) would increase the slope.

4.5. The Dependence of the $M_{\text{BH}} - \sigma_*$ Relation on the Eddington Ratio and Redshift

The distribution of data points in the $M_{\text{BH}} - \sigma_*$ plane may be affected by many factors, such as the details of the BLR physics and galaxy evolution. We can begin to examine the dependence of the distribution of points in the plane on some of these factors, at least in a statistical sense, thanks to the large size of our data set.

Figure 25 shows the $M_{\text{BH}} - \sigma_*$ relationship for two different ranges of $L_{\text{bol}}/L_{\text{Edd}}$. The AGN sample was divided at the median value of the Eddington ratio, $L_{\text{bol}}/L_{\text{Edd}} = 0.027$. Objects with $L_{\text{bol}}/L_{\text{Edd}}$ values below the median are shown as filled squares, and those with values above the median are shown as open triangles. The median values for the low and high $L_{\text{bol}}/L_{\text{Edd}}$ groups are 0.015 and 0.072 respectively. Each point represents the mean value for at least 25 objects. There is a clear separation in the $M_{\text{BH}} - \sigma_*$ relationship between the high and low $L_{\text{bol}}/L_{\text{Edd}}$ samples. For a given velocity dispersion, those objects with lower values of $L_{\text{bol}}/L_{\text{Edd}}$ have larger black hole masses. The slopes of the relationship in the

two samples are not significantly different, but the intercepts differ greatly. With the slope fixed at 4.02 as for inactive galaxies, the intercepts are 8.15 ± 0.02 and 7.68 ± 0.02 for the samples with low and high $L_{\text{bol}}/L_{\text{Edd}}$ respectively. The intercepts differ by about 0.47 dex in $\log(M_{\text{BH}})$ in the two groups. The intercept of the low $L_{\text{bol}}/L_{\text{Edd}}$ sample is a bit higher than that of inactive galaxies (Tremaine et al. 2002), which of course have extremely low $L_{\text{bol}}/L_{\text{Edd}}$ values. Generally then, in the sample studied here, BH masses are smaller relative to the mean relation for objects with larger Eddington ratios.

The 0.47 dex difference of the intercepts in the two groups is statistically significant ($> 10\sigma$), given the precision with which they can be measured with the large samples. At face value, this result would tie together the accretion rate with physical properties of the host bulge component. However, there may be selection effects and parameter interdependencies that could cause the apparent difference. For example, Fig. 15 shows an anticorrelation between M_{BH} and $L_{\text{bol}}/L_{\text{Edd}}$, but as discussed in § 3.5, it is caused by selection effects and the functional interdependence of the two parameters. Therefore, to determine the reality of the apparent dependence of the $M_{\text{BH}} - \sigma_*$ relationship on $L_{\text{bol}}/L_{\text{Edd}}$, correlations among the other parameters that are involved — AGN monochromatic luminosity L_{5100} , emission line FWHM, host luminosity L_H , stellar velocity dispersion σ_* , and redshift — must be taken into account. To test the reality of the results, we have used partial correlation analysis to account for the interdependencies.

For the partial correlation tests, we defined a new variable ΔM_{BH} ,

$$\Delta M_{\text{BH}} = \log(M_{\text{BH}}) - 3.34 \log(\sigma_*/200 \text{ km s}^{-1}) - 7.92, \quad (10)$$

which is the difference, in logarithmic space, between the measured BH mass and the BH mass predicted by equation (8). Fig. 26 shows the relationship between ΔM_{BH} and Eddington ratio; there is apparently a strong anti-correlation, with a Pearson product-moment correlation coefficient of -0.576 . A partial correlation analysis (e.g. Wall & Jenkins 2003) was performed on ΔM_{BH} and $L_{\text{bol}}/L_{\text{Edd}}$, controlling for L_{5100} , FWHM, σ_* , L_H , and redshift; the analysis was performed in logarithmic space, because many of the relationships are then more closely linear. The results are shown in Table 3. Each row of Table 3 shows the ΔM_{BH} vs. $L_{\text{bol}}/L_{\text{Edd}}$ partial correlation coefficient, $r_{\Delta M, \text{Eratio}; x}$, where x is one of the control variables, and the probability that such a coefficient value or less would occur by chance. Controlling for each of the other variables, there is less than a 0.01% probability that the ΔM_{BH} anti-correlation with Eddington ratio is due to chance. Table 3 lists the correlation coefficients, $r_{\text{Eratio}, x}$ and $r_{\Delta M, x}$, between Eddington ratio and ΔM_{BH} respectively, and the control variables. It is easy to show from the partial correlation results that the anti-correlation of ΔM_{BH} with $L_{\text{bol}}/L_{\text{Edd}}$ is not due to the interdependencies of M_{BH} , L_{5100} , and $L_{\text{bol}}/L_{\text{Edd}}$. For a fixed $FWHM$, both M_{BH} and $L_{\text{bol}}/L_{\text{Edd}}$ are positively correlated with

L_{5100} , by their definitions. Thus, by equation (10), one would expect a positive correlation between ΔM_{BH} and $L_{\text{bol}}/L_{\text{Edd}}$ for a given $FWHM$, assuming no other dependencies. However, the partial correlation coefficient, controlling for $FWHM$, is negative (Table 3) and still highly significant. Therefore, the anti-correlation of ΔM_{BH} with $L_{\text{bol}}/L_{\text{Edd}}$ is not due to the interdependencies of M_{BH} , L_{5100} , and $L_{\text{bol}}/L_{\text{Edd}}$.

The partial correlation tests do not determine whether the ΔM_{BH} vs. $L_{\text{bol}}/L_{\text{Edd}}$ anti-correlation is due to sample selection effects. Figure 27 shows that there is a correlation between AGN monochromatic luminosity and host galaxy velocity dispersion, with a correlation coefficient of 0.569. This correlation can explain the difference between the intercepts in Fig. 25. For a given BH mass, objects with larger values of σ_* will generally have larger values of L_{5100} , and therefore, larger Eddington ratios. Therefore, objects to the right of the regression line (having larger σ_* values) will generally have larger Eddington ratios, and vice versa. However, the correlation between L_{5100} and σ_* may be a consequence of the Faber-Jackson relation (§ 4.2, Fig. 20) and a correlation between L_{5100} and host luminosity L_H , shown in Fig. 28 (cf. VB06). Assuming the Faber-Jackson relation we see is not due to selection effects, the reality of the $M_{\text{BH}} - \sigma_*$ dependence on the Eddington ratio depends upon whether or not the $L_{5100} - L_H$ correlation is intrinsic, or due to selection effects. As discussed by VB06, at least part of the correlation is due to the restriction that both the host and AGN components contribute significantly to the composite spectrum; this corresponds to the $0.2 < F_H < 0.8$ criteria described in § 2. There are clearly many AGNs in the universe that do not satisfy those criteria. The partial correlation coefficients of AGN monochromatic luminosity and host galaxy velocity dispersion are shown in Table 4. Although the correlation is weaker controlling for L_H and/or redshift, it is still significant. Hence, the correlation of AGN monochromatic luminosity and host galaxy velocity dispersion is intrinsic, but is enhanced due to a sample selection effect. To summarize, the apparent $M_{\text{BH}} - \sigma_*$ dependence on $L_{\text{bol}}/L_{\text{Edd}}$ remains after accounting for several possible interdependencies, although it is likely that the relative luminosity criteria used to construct the spectroscopic sample artificially strengthens the apparent dependence.

Selection effects similar to ones imposed on the spectroscopic sample can be avoided, at least partially, in high-resolution imaging studies, such as those carried out with the *HST* (e.g. Floyd et al. 2004; Sánchez et al. 2004; Dunlop et al. 2003; Pagani et al. 2003; Hamilton et al. 2002; Schade et al. 2000). In a recent compilation by Sánchez et al. (2004), for example, a strong correlation was found between nuclear and host luminosities. The explanation is that the data are bracketed by lines of constant Eddington luminosity, ranging from $L_{\text{bol}}/L_{\text{Edd}} \approx 0.01$ to 1. The cutoff at an Eddington ratio of near unity is particularly sharp, possibly indicating that very few AGNs emit above their Eddington limit. The low Eddington ratio limit is more likely to be a selection effect, in that low-luminosity nuclei are

difficult to detect in high-luminosity hosts. The apparent correlation, whether intrinsic or a selection effect, would cause at least qualitatively the same dependence of the $M_{\text{BH}} - \sigma_*$ relation on the Eddington ratio seen in Fig. 25.

Figure 29 shows the $M_{\text{BH}} - \sigma_*$ relationship for data in several different redshift bins. Our sample was divided into three subgroups by redshift: $0 < z < 0.1$, $0.1 < z < 0.2$, and $z > 0.2$, shown in the figure by open triangles, filled squares, and crosses respectively. The data were separated into bins of host M_g , as with the previous analysis; each point represents data from at least 25 objects. The points clearly occupy different regions along the best fit $M_{\text{BH}} - \sigma_*$ line. That is due to the redshift-luminosity selection effect correlation in the sample, seen in Fig. 3: objects at higher redshifts have higher luminosities on average, so AGNs with larger host velocity dispersions and more massive black holes are preferentially selected at higher redshifts. The solid line shows the best fit to the $M_{\text{BH}} - \sigma_*$ relation from equation (8). Figure 29 shows that the intercept of the relationship doesn't change greatly with redshift. The points in the highest redshift bin are on average slightly above the best fit line, while those at lower redshifts are slightly below the line on average, suggesting a possible redshift evolution of the $M_{\text{BH}} - \sigma_*$ relation. With the slope fixed to the value in equation (8), the intercepts of the three groups from low to high redshifts are 7.85 ± 0.02 , 7.88 ± 0.02 and 8.00 ± 0.03 respectively. At face value, the results suggest a weak but significant dependence of the $M_{\text{BH}} - \sigma_*$ relation on redshift, such that active galaxies on average have larger black hole masses for a given velocity dispersion at high redshift as compared to low redshift.

As with the dependence of the $M_{\text{BH}} - \sigma_*$ relation on Eddington ratio, a partial correlation analysis was performed to determine whether the apparent redshift dependence of ΔM_{BH} could be accounted for by correlations with other parameters. The correlation coefficient of ΔM_{BH} with redshift, not accounting for other parameters, is 0.005 (see last row of Table 3), which is relatively small but may or may not be significant. The results of the partial correlation analysis, with L_{5100} , FWHM, σ_* , L_H , and $L_{\text{bol}}/L_{\text{Edd}}$ as the control variables, are shown in Table 5. For each of the control variables, the remaining correlation between ΔM_{BH} and redshift is relatively small. The significance of the remaining correlations are all quite high (probabilities $< 0.11\%$), except when L_H is the control variable, in which case the probability of a chance correlation is about 11.8%. However, when controlling for all five parameters, the partial correlation coefficient is 0.059 with a random probability of being greater of 92.4%. Thus, there is no compelling evidence for redshift evolution in the $M_{\text{BH}} - \sigma_*$ relation for the sample presented here.

The lack of evidence for redshift evolution is in contrast to the results of several studies (Treu et al. 2004; Woo et al. 2006; Peng et al. 2006a,b; Shields et al. 2006), that have found apparent positive correlations between the $M_{\text{BH}} - \sigma_*$ relation and redshift. Woo et al. (2006)

found that their sample of Seyfert galaxies at $z \approx 0.36$ had larger black hole masses for a given σ_* , relative to the values expected from the local relation. Shields et al. (2006) measured CO emission lines to infer σ_* for a set of nine high-redshift AGNs, and found that the host masses are undersized by more than an order of magnitude, given their BH masses. Peng et al. (2006a,b) found that $z \gtrsim 2$ hosts in their sample are less luminous (and therefore less massive) than expected for a given M_{BH} . In contrast, Shields et al. (2003) and Salviander et al. (2006), using O [III] line widths as surrogates for σ_* , found no evidence for redshift evolution up to $z \sim 3$. There is also evidence from a study of high-redshift sub-millimeter galaxies (Borys et al. 2005) that at least some galaxies at high redshift have BH masses substantially *smaller* than expected for their host masses. The methods and equations used to estimate M_{BH} and σ_* were somewhat different in each study, and different from our own, and each sample was selected in different ways, so direct comparisons are not necessarily valid. Our study is the first to examine the possibility of redshift evolution for a single, large, homogeneously collected and analyzed sample spanning both low and relatively high redshifts; and our study is the first to determine whether an apparent dependence of the redshift evolution could be the result of correlations among other parameters. It will be important to extend the studies of the $M_{\text{BH}} - \sigma_*$ relation to higher redshifts, over a wide range of BH masses and velocity dispersions, using a variety of techniques.

5. Discussion and Summary

The very large and homogeneous data set analyzed here has allowed parameterization of several relations for broad-line active galaxies. Host galaxy luminosity and velocity dispersion are described by the Faber-Jackson relation, central black hole mass is correlated with host bulge luminosity and velocity dispersion, the amplitude of the $M_{\text{BH}} - \sigma_*$ relation depends inversely on the Eddington ratio, and there is no significant change in the $M_{\text{BH}} - \sigma_*$ relation with redshift up to $z \approx 0.4$.

The dependence of the $M_{\text{BH}} - \sigma_*$ relation on both redshift and Eddington ratio have been matters of dispute. In our sample, we find no significant correlation with redshift after accounting for possible correlations among many other parameters. As discussed in § 4.5, there are studies that support positive, negative, and no correlation with redshift. The $M_{\text{BH}} - \sigma_*$ relation appears to depend on the Eddington ratio, even after accounting for other parameters. Apparently, the difference we have found between the high and low $L_{\text{bol}}/L_{\text{Edd}}$ samples is sufficient to account for the intrinsic scatter in the $M_{\text{BH}} - \sigma_*$ relation, usually measured to be about 0.4 dex in black hole mass for a given velocity dispersion (e.g. Greene & Ho 2006a, § 4 of this paper). We checked this result by dividing the Greene & Ho

(2006a) sample by its median $L_{\text{bol}}/L_{\text{Edd}}$; this sample shows the same qualitative trend that objects with higher Eddington ratios have smaller black hole masses for a given velocity dispersion (although the uncertainty is too great to say whether it can account for the scatter). As discussed in §4.5, the dependence of the $M_{\text{BH}} - \sigma_*$ relation on $L_{\text{bol}}/L_{\text{Edd}}$ is probably at least partly due to selection effects — which may also affect the Greene & Ho (2006a) sample — but a significant intrinsic component cannot be ruled out.

There is other observational support for an anti-correlation between the $M_{\text{BH}} - \sigma_*$ relation and Eddington ratio from observations of narrow-line Seyfert 1 galaxies (NLS1s). These active galaxies typically have relatively small measured BH masses and high accretion rates, which results in large Eddington ratios. Several studies (e.g. Wandel 2002; Grupe & Mathur 2004; Bian & Zhao 2004; Nelson et al. 2004) have shown that NLS1s tend to lie below the $M_{\text{BH}} - \sigma_*$ relation for inactive galaxies. If NLS1s are an early stage of AGN evolution, then they will presumably move up the $M_{\text{BH}} - \sigma_*$ plane over time (BH masses growing), becoming broad-line AGNs and eventually inactive galaxies harboring supermassive black holes. If the objects evolve in this way toward the $z = 0$ $M_{\text{BH}} - \sigma_*$ relation, the black holes would have to be growing more rapidly than the bulges are growing. To explain the tight relationship between the final BH and spheroid masses, the gas mass that builds the black hole may somehow be set at a given formation stage of the stellar spheroid. It would then be the fate of the black hole to grow to a particular mass, determined very early in its development by the mass of the spheroid (e.g. Miralda-Escudé & Kollmeier 2005; Merritt & Poon 2004). Feedback from the central engine surrounding the BH may regulate the BH growth process (e.g. Robertson et al. 2006; Begelman & Nath 2005; Di Matteo et al. 2005; King 2003), but this feedback may have little to do with the development of the spheroid. It is also possible that NLS1s are not a representative class of AGN, and their evolutionary tracks in the $M_{\text{BH}} - \sigma_*$ plane are different than those of other types. Observations of AGNs with luminosities comparable to NLS1s, but at higher redshifts than can be obtained with the SDSS, would help clarify the issue.

Differences in the $M_{\text{BH}} - \sigma_*$ relation may also be due to disk orientation effects, which could produce a wide range of incorrect estimates for black hole masses. Given that all BH masses were determined by using the same value of the f factor (equation 1), the objects with high $L_{\text{bol}}/L_{\text{Edd}}$ may be those in which BH masses are underestimated because their true f values are larger. McLure & Dunlop (2001, 2002) argue that a flattened-disk-like geometry in the BLR is favored over randomly-oriented orbits, and a flattened geometry viewed over a range of orientation angles can easily result in virial BH masses underestimated by a factor of three. However, Collin et al. (2006) showed that the inclination effects are actually minimal when using the line dispersions as opposed to the FWHM of the line profile. Although the factor of 3 difference in the BH masses (0.5 dex) can explain the apparent dependence of

the $M_{\text{BH}} - \sigma_*$ relation on $L_{\text{bol}}/L_{\text{Edd}}$, we cannot settle this issue here because of our poor understanding of the BLR geometry.

Our BH masses were estimated by equation (2), where FWHM was used to characterize the line width (Vestergaard & Peterson 2006)). However, some studies showed that the line dispersion is a less biased parameter in general than FWHM for black hole mass estimation (e.g. Peterson et al. 2004; Collin et al. 2006). The line dispersion will also minimize the effect that may be influenced by relative source inclination (Collin et al. 2006).

The SDSS spectroscopic data set has provided a large sample of homogeneously selected AGN from which both nuclear and host properties can be measured. The moderate resolution and S/N of the SDSS spectra limit the ranges of accessible luminosities, black hole masses, and Eddington ratios. However, in principle, the eigenspectrum decomposition technique can be applied to any spectrum with adequately strong nuclear and host components, so it is possible with other data sets to extend the results of this study to a larger dynamic range.

We thank Todd Boroson for providing the iron template, and Smita Mathur, Dirk Grupe, Christy Tremonti, Ching-Wa Yip, Mariangela Bernardi, Ohad Shemmer, David Schlegel, and Jenny Greene for useful discussion. This research was partially supported by NSF grants AST03-07582 and AST06-07634. P.B.H. is supported by NSERC.

Funding for the SDSS and SDSS-II has been provided by the Alfred P. Sloan Foundation, the Participating Institutions, the National Science Foundation, the U.S. Department of Energy, the National Aeronautics and Space Administration, the Japanese Monbukagakusho, the Max Planck Society, and the Higher Education Funding Council for England. The SDSS Web Site is <http://www.sdss.org/>. The SDSS is managed by the Astrophysical Research Consortium for the Participating Institutions. The Participating Institutions are the American Museum of Natural History, Astrophysical Institute Potsdam, University of Basel, Cambridge University, Case Western Reserve University, University of Chicago, Drexel University, Fermilab, the Institute for Advanced Study, the Japan Participation Group, Johns Hopkins University, the Joint Institute for Nuclear Astrophysics, the Kavli Institute for Particle Astrophysics and Cosmology, the Korean Scientist Group, the Chinese Academy of Sciences (LAMOST), Los Alamos National Laboratory, the Max Planck-Institute for Astronomy (MPIA), the Max-Planck-Institute for Astrophysics (MPA), New Mexico State University, Ohio State University, University of Pittsburgh, University of Portsmouth, Princeton University, the United States Naval Observatory, and the University of Washington.

REFERENCES

- Abazajian, K., et al. 2005, *AJ*, 129, 1755
- Akritas, M.G., & Bershad, M.A. 1996, *ApJ*, 470, 706
- Anderson, S. F., et al. 2003, *AJ*, 126, 2209
- Barth, A., Ho, L., & Sargent, W.L.W. 2002, *ApJ*, 566, L13
- Barth, A.J., Ho, L.C., Rutledge, R.E., & Sargent, W.L.W. 2004 *ApJ*, 607, 90
- Barth, A.J., Greene, J.E., & Ho, L.C. 2005, *ApJ*, 619, L151
- Becker, R. H., White, R. L., & Helfand, D. J. 1995, *ApJ*, 450, 559
- Begelman, M. C., & Nath, B. B. 2005, *MNRAS*, 361, 1387
- Bender, R. 1990, *A&A*, 229, 441
- Bentz, M.C. et al. 2006, *ApJ*, 644, 133
- Bernardi, M., et al. 2003a, *AJ*, 125, 1817
- Bernardi, M., et al. 2003b, *AJ*, 125, 1849
- Bian, W., & Zhao, Y. 2004, *MNRAS*, 347, 607
- Blandford, R.D., & McKee, C.F. 1982, *ApJ*, 255, 419
- Blanton, M. R., Lin, H., Lupton, R. H., Maley, F. M., Young, N., Zehavi, I., & Loveday, J. 2003, *AJ*, 125, 2276
- Bonning, E. W., Shields, G. A., Salviander, S., & McLure, R. J. 2005, *ApJ*, 626, 89
- Boroson, T.A., & Green, R.F. 1992, *ApJS*, 80, 109
- Boroson, T.A. 2003, *ApJ*, 585, 647
- Boroson, T. 2005, *AJ*, 130, 381
- Borys, C., Smail, I., Chapman, S. C., Blain, A. W., Alexander, D. M., & Ivison, R. J. 2005, *ApJ*, 635, 853
- Botte, V., Ciroi, S., di Mille, F., Rafanelli, P., & Romano, A. 2005, *MNRAS*, 356, 789
- Brinchmann, J., et al. 2004, *astro-ph/0406220*

- Collin, S., Kawaguchi, T., Peterson, B. M., & Vestergaard, M. 2006, *A&A*, 456, 75
- Connolly, A. J., & Szalay, A. S. 1999, *AJ*, 117, 2052
- Di Matteo, T., Springel, V., & Hernquist, L. 2005, *Nature*, 433, 604
- Dunlop, J. S., McLure, R. J., Kukula, M. J., Baum, S. A., O’Dea, C. P., & Hughes, D. H. 2003, *MNRAS*, 340, 1095
- Faber, S.M., & Jackson, R.E. 1976, *ApJ*, 204, 668
- Ferrarese, L., & Merritt, D. 2000, *ApJ*, 539, L9
- Ferrarese, L., Pogge, R. W., Peterson, B. M., Merritt, D., Wandel, A., & Joseph, C. L. 2001, *ApJ*, 555, L79
- Fitzpatrick, E.L. 1999, *PASP*, 111, 63
- Floyd, D. J. E., Kukula, M. J., Dunlop, J. S., McLure, R. J., Miller, L., Percival, W. J., Baum, S. A., & O’Dea, C. P. 2004, *MNRAS*, 355, 196
- Franx, M., Illingworth, G.D., & Heckman, T. 1989, *ApJ*, 344, 613
- Fukugita, M., Ichikawa, T., Gunn, J.E., Doi, M., Shimasaku, K., & Schneider, D.P. 1996, *AJ*, 111, 1748
- Gebhardt, K., et al. 2000, *ApJ*, 539, L13
- Greene, J.E., & Ho L.C. 2005, *ApJ*, 630, 122
- Greene, J.E., & Ho L.C., 2006a, *ApJ*, 641, L21
- Greene, J.E., & Ho L.C. 2006b, *ApJ*, 641, 117
- Grupe, D., & Mathur, S. 2004, *ApJ*, 606, L41
- Gunn, J.E., et al. 1998, *AJ*, 116 3040
- Gunn, J.E., et al. 2006, *AJ*, 131, 2332
- Hamilton, T. S., Casertano, S., & Turnshek, D. A. 2002, *ApJ*, 576, 61
- Heckman T., et al. 2004, *ApJ*, 613, 109
- Hogg, D. W., Schlegel, D. J., Finkbeiner, D. P., & Gunn, J. E. 2001, *AJ*, 122, 2129

- Ivezić, Ž., et al. 2002, *AJ*, 124, 2364
- Jørgensen I., Franx, M., & Kjaergaard, P. 1995, *MNRAS*, 276, 1341
- Kaspi, S., Smith P.S., Netzer, H., Maoz, D., Jannuzi, B.T., & Giveon, U. 2000, *ApJ*, 533, 631
- Kaspi, S., Maoz, D., Netzer, H., Peterson, B.M., Vestergaard, M., & Jannuzi, B.T. 2005, *ApJ*, 629, 61
- King, A. 2003, *ApJ*, 596, L27
- Kollatschny, W. 2003, *A&A*, 407, 461
- Kormendy, J., & Richstone, D. 1995, *ARA&A*, 33, 581
- Kuhlbrodt, B., Wisotzki, L., & Jahnke, K. 2004, *MNRAS*, 349, 1027
- Laor, A. 1998, *ApJ*, 505, L83
- Lynden-Bell, D. 1969, *Nature*, 223, 690
- Magorrian, J., et al. 1998, *AJ*, 115, 2285
- McLure, R.J., Dunlop, J.S., & Kukula, M.J. 2000, *MNRAS*, 318, 693
- McLure, R.J., & Dunlop, J.S. 2001, *MNRAS*, 327, 199
- McLure, R.J., & Dunlop, J.S. 2002, *MNRAS*, 331, 795
- McLure, R.J., & Jarvia, M.J. 2002, *MNRAS*, 337, 109
- Merritt, D., & Poon, M. Y. 2004, *ApJ*, 606, 788
- Miralda-Escudé, J., & Kollmeier, J. A. 2005, *ApJ*, 619, 30
- Moultaka, J., Ilovaisky, S.A., Prugniel, P. & Soubiran, C. 2004, *PASP*, 116, 693
- Murray, N., & Chiang, J. 1997, *ApJ*, 474, 91
- Nelson, C. H., & Whittle, M. 1996, *ApJ*, 465, 96
- Nelson, C.H. 2000, *ApJ*, 544, L91
- Nelson, C.H., Green, R.F., Bower, G., Gebhardt, K., & Weistrop, D. 2004, *ApJ*, 615, 652

- Netzer, H., & Peterson, B. M. 1997, in *Astronomical Time Series*, ed. D. Maoz, A. Sternberg, & E. M. Leibowitz (Dordrecht: Kluwer), 85
- Netzer, H. 2003, *ApJ*, 583, L5
- Onken, C.A., & Peterson, B.M. 2002, *ApJ*, 572, 746
- Onken, C.A., Ferrarese, L., Merritt, D., Peterson, B.M., Pogge, R.W., Vestergaard, M., & Wandel, A. 2004, *ApJ*, 615, 645
- Pagani, C., Falomo, R., & Treves, A. 2003, *ApJ*, 596, 830
- Peng, C.Y., Ho, L.C., Impey, C.D., & Rix, H. 2002, *AJ*, 124, 266
- Peng, C. Y., Impey, C. D., Ho, L. C., Barton, E. J., & Rix, H.-W. 2006a, *ApJ*, 640, 114
- Peng, C. Y., Impey, C. D., Rix, H.-W., Kochanek, C. S., Keeton, C. R., Falco, E. E., Lehár, J., & McLeod, B. A. 2006b, *ApJ*, 649, 616
- Peterson, B.M. 1993, *PASP*, 105, 247
- Peterson, B.M., & Wandel, A. 1999, *ApJ*, 521, L95
- Peterson, B.M., & Wandel, A. 2000, *ApJ*, 540, L13
- Peterson, B.M., et al. 2004, *ApJ*, 613, 682
- Peterson, B.M., et al. 2005, *ApJ*, 632, 799
- Pier, J. R., Munn, J. A., Hindsley, R. B., Hennessy, G. S., Kent, S. M., Lupton, R. H., & Ivezić, Ž. 2003, *AJ*, 125, 1559
- Press, W. H., Teukolsky, S. A., Vetterling, W. T., & Flannery, B. P. 1992, *Numerical Recipes in C* (Second ed.; cambridge: Cambridge Univ. Press), 660
- Rees, M. J. 1984, *ARA&A*, 22, 471
- Richards, G. T. et al. 2002, *AJ*, 123, 2945
- Richards, G. T. et al. 2006, *astro-ph/0601558*
- Rix, H.W., & White, S.D.M. 1992, *MNRAS*, 254, 389
- Robertson, B., Hernquist, L., Cox, T. J., Di Matteo, T., Hopkins, P. F., Martini, P., & Springel, V. 2006, *ApJ*, 641, 90

- Salviander, S., Shields, G. A., Gebhardt, K., & Bonning, E. W. 2006, *New Astronomy Review*, 50, 803
- Sánchez, S. F., et al. 2004, *ApJ*, 614, 586
- Sargent, W.L.W., Schechter, P.L., Boksenberg, A., & Shortridge, K. 1977, *ApJ*, 212, 326
- Schade, D. J., Boyle, B. J., & Letawsky, M. 2000, *MNRAS*, 315, 498
- Schlegel, D.J., Finkbeiner, D.P., & Davis, M. 1998, *ApJ*, 500, 525
- Schneider, D.P. et al. 2005, *AJ*, 130, 367
- Shang, Z. et al. 2005, *ApJ*, 619, 41
- Shields, G.A., Gebhardt, K., Salviander, S., et al. 2003, *ApJ*, 583, 124
- Shields, G. A., Menezes, K. L., Massart, C. A., & Vanden Bout, P. 2006, *ApJ*, 641, 683
- Smith, J. A., et al. 2002, *AJ*, 123, 2121
- Spergel, D.N. et al. 2006, *astro-ph/0603449*
- Stoughton, C. et al. 2002, *AJ*, 123, 485
- Strauss, M. A. et al. 2002, *AJ*, 124, 1810
- Tonry, J., & Davis, M. 1979, *AJ*, 84, 1511
- Tremaine, S., et al. 2002, *ApJ*, 574, 740
- Treu, T., Malkan, M. A., & Blandford, R. D. 2004, *ApJ*, 615, L97
- Vanden Berk, D. E., et al. 2005, *AJ*, 129, 2047
- Vanden Berk, D. E., Shen, J., Yip, C.-W., Schneider, D. P., et al. 2006, *AJ*, 131, 84
- Vestergaard, M. 2002, *ApJ*, 571, 733
- Vestergaard, M. 2004, *ApJ*, 601, 676
- Vestergaard, M., & Peterson, B.M. 2006, *ApJ*, 641, 689
- Wall, J.V. & Jenkins C.R. 2003, *Practical Statistics for Astronomers*, P66, Cambridge University Press
- Wandel, A., Peterson, B.M., & Malkan, M.A. 1999 *ApJ*, 526, 579

- Wandel, A. 2002, ApJ, 565, 762
- Warner, C., Hamann, F., & Dietrich, M. 2003, ApJ, 596, 72
- Wegner, G., Colless, M., Saglia, R. P., McMahan, R. K., Davies, R. L., Burstein, D., & Baggle, G. 1999, MNRAS, 305, 259
- Woo, J.-H., Treu, T., Malkan, M. A., & Blandford, R. D. 2006, ApJ, 645, 900
- Wu, X.B., Wang, R., Kong, M.Z., Liu, F.K., & Han, J.L. 2004, A&A
- Véron-Cetty, M.-P., Joly, M., & Véron, P. 2004, A&A, 417, 515
- Yip, C.W., et al. 2004a, AJ, 128, 585
- Yip, C.W., et al. 2004b, AJ, 128, 2603
- York, D.G., et al. 2000, AJ, 120, 1579

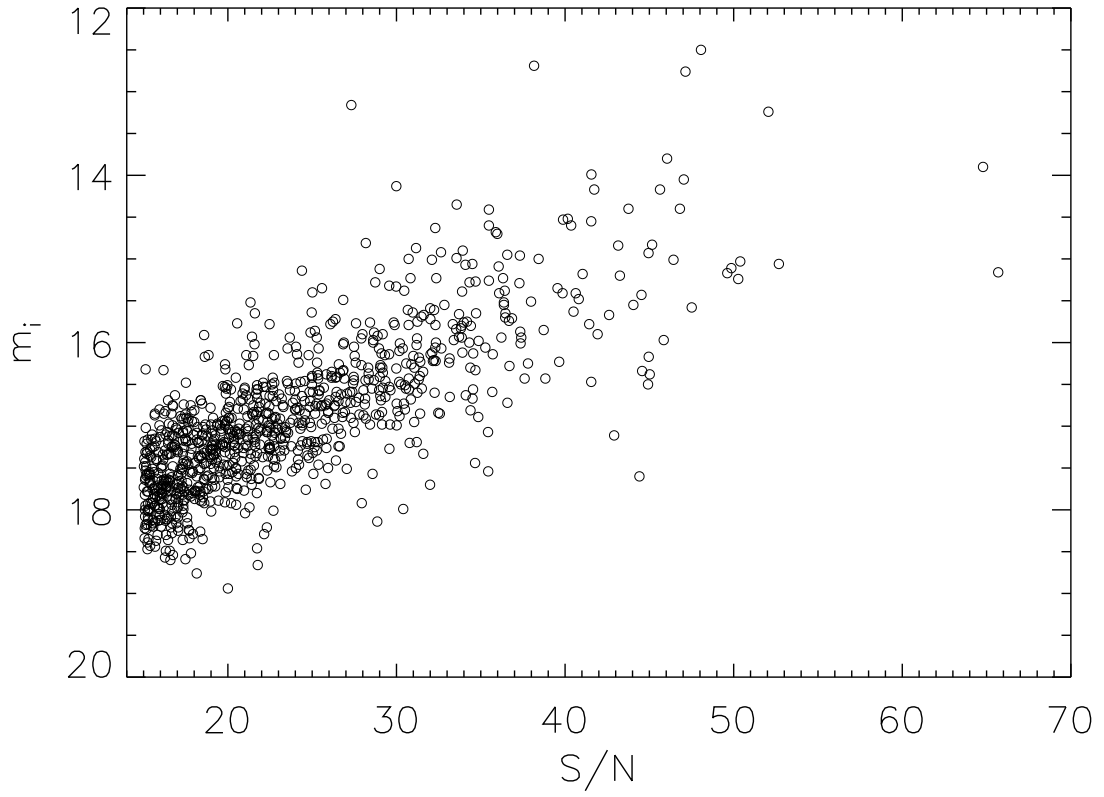


Fig. 1.— Sample object apparent i band magnitudes m_i vs. the spectroscopic S/N averaged over the i band. The median S/N is 21.6.

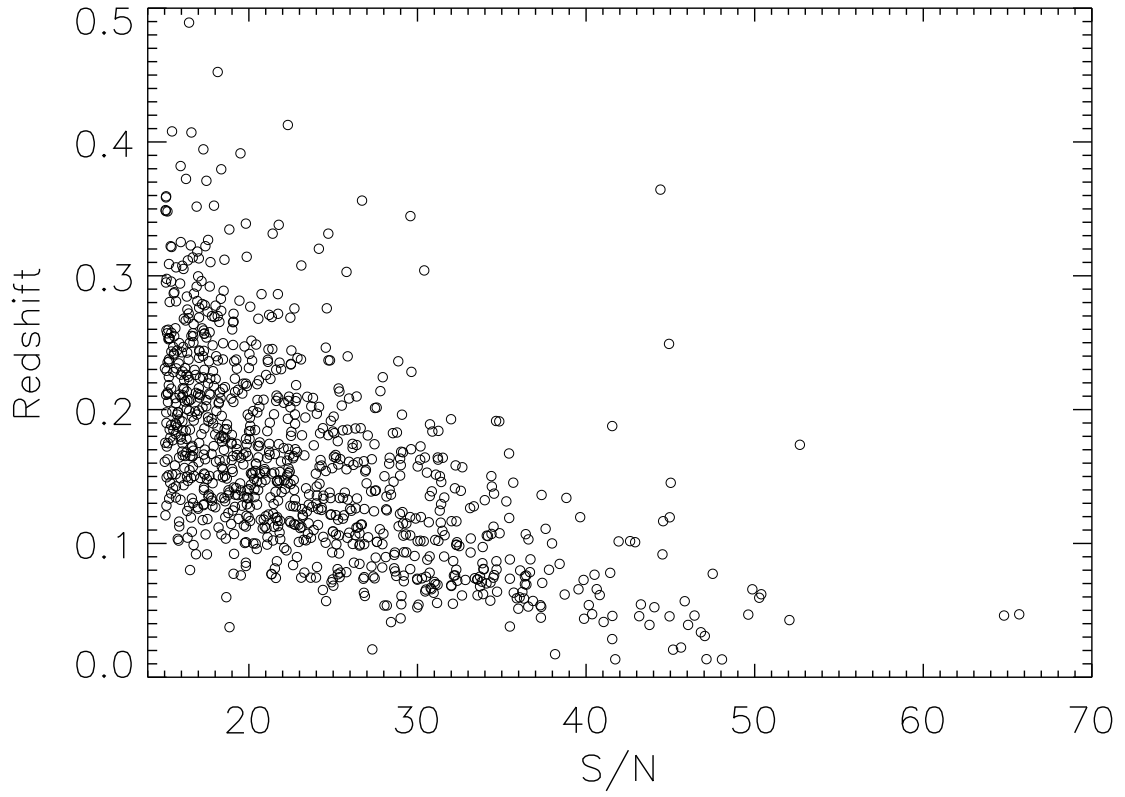


Fig. 2.— Sample object redshift vs. the spectroscopic S/N averaged over the i band.

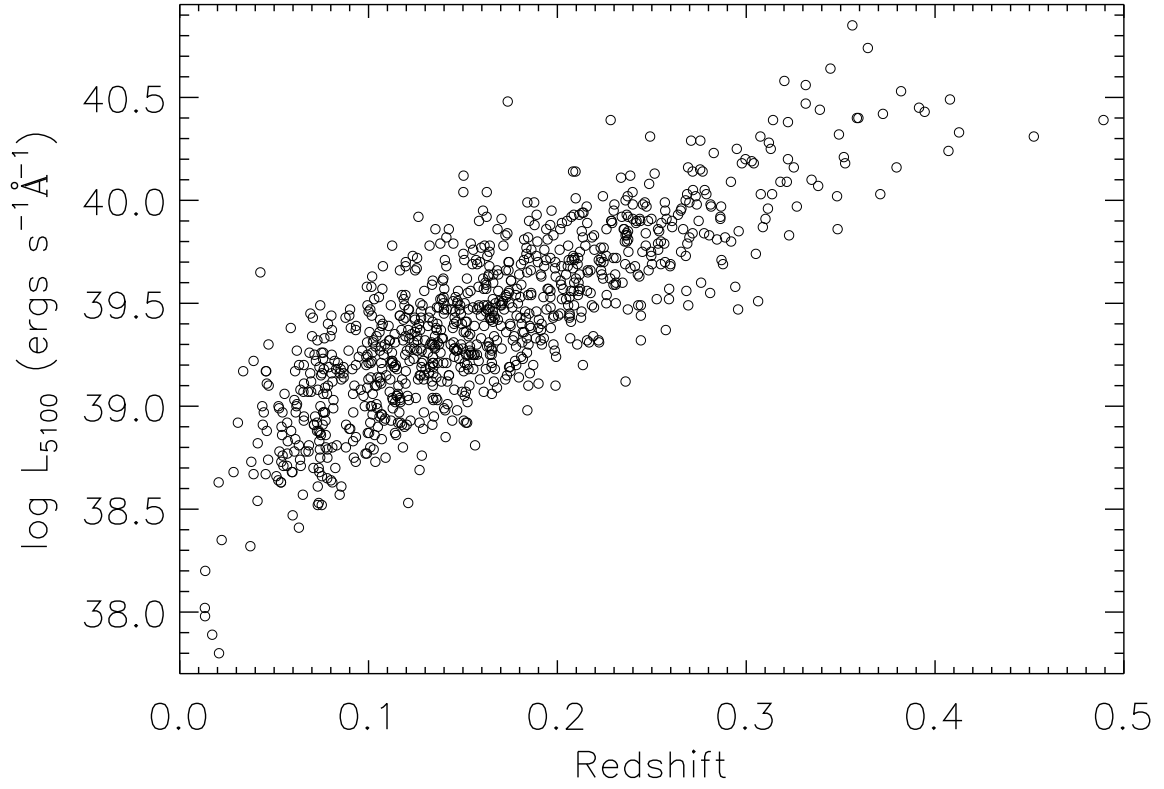


Fig. 3.— AGN monochromatic continuum luminosity at a rest wavelength of 5100\AA , L_{5100} , as a function of redshift for the 960 objects in our sample. The AGN luminosity was measured after host galaxy subtraction; the measurement of this quantity is discussed in § 3.1.

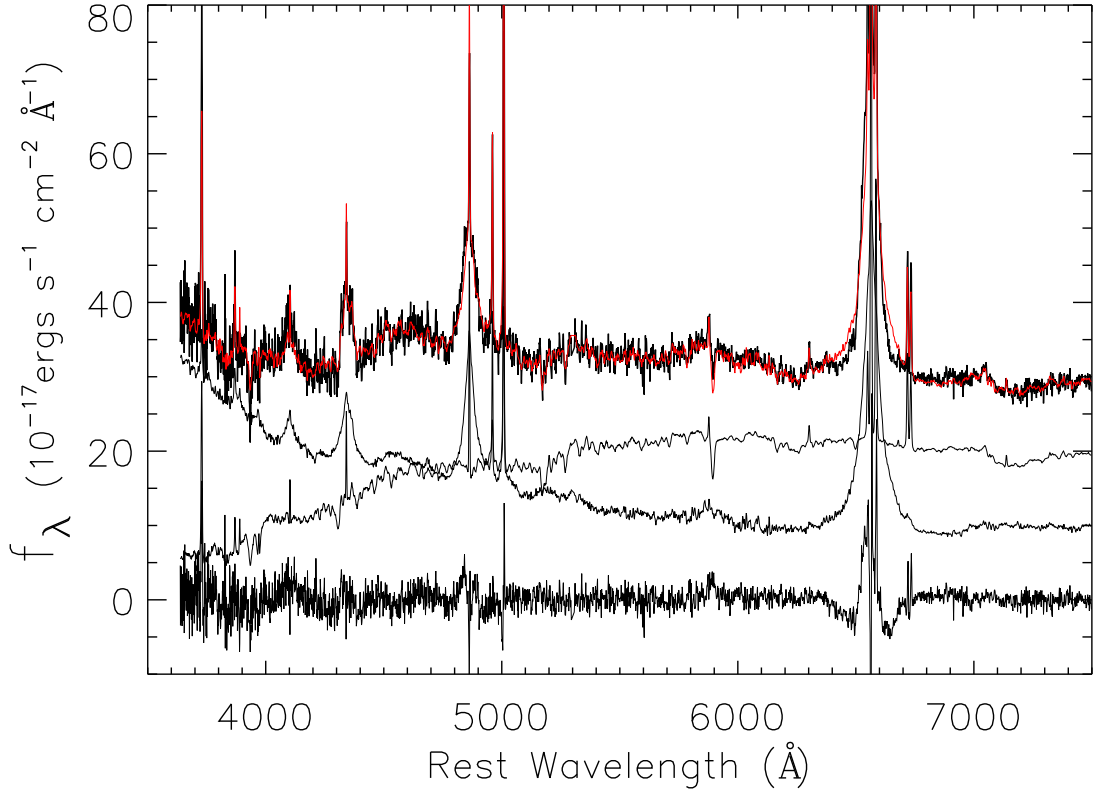


Fig. 4.— The SDSS spectrum of SDSS J104252.94+041441.1, with $z = 0.053$, a typical example of a high- S/N object in our sample, with $S/N = 37.3$ (the spectra have a resolution of $\Delta\lambda/\lambda \sim 1850$). The middle components are the *reconstructed* AGN and host galaxy spectra, the top histogram is the original active galaxy spectrum, and the bottom histogram is the fit residual. The gray curve is the modeled active galaxy spectrum, which is red in the electronic version.

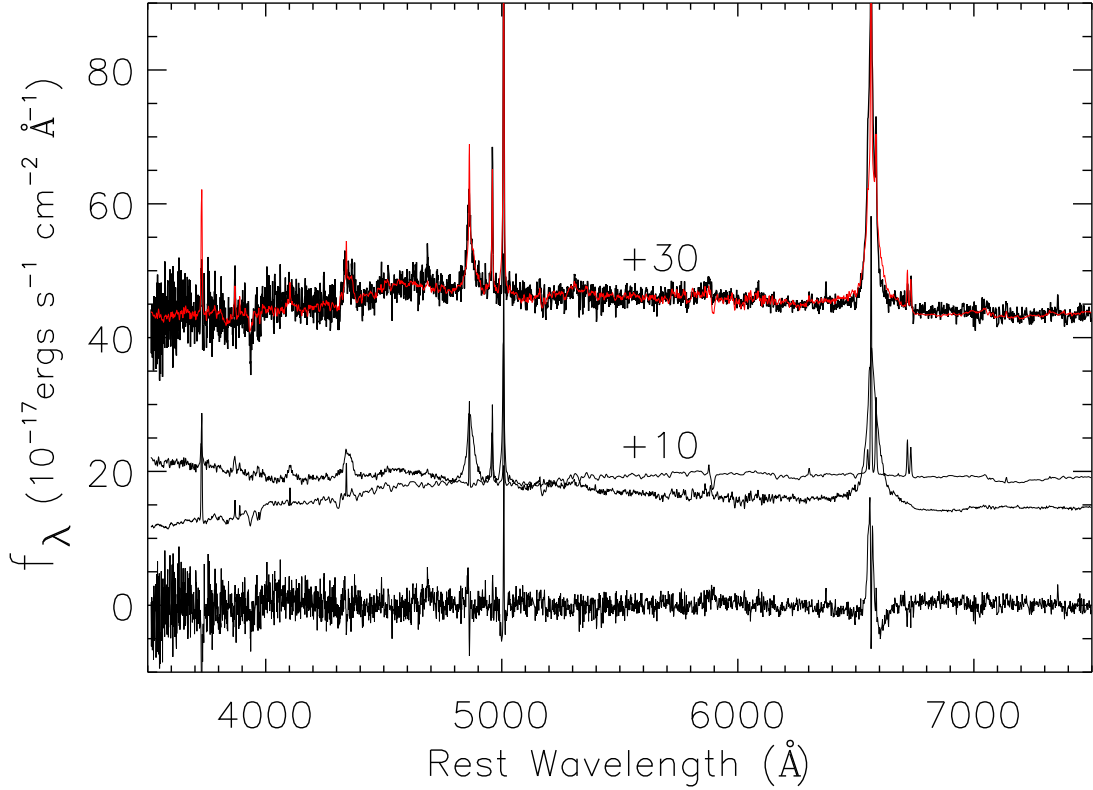


Fig. 5.— The SDSS spectrum of SDSS J212348.61+105348.2, with $z = 0.087$, a typical example of an object with average S/N in our sample, with $S/N = 21.7$. The middle components are the *reconstructed* AGN and host galaxy spectra with an offset for clarity, the top histogram is the original active galaxy spectrum with an offset for clarity, and the bottom histogram is the fit residual. The gray curve is the modeled active galaxy spectrum, which is red in the electronic version.

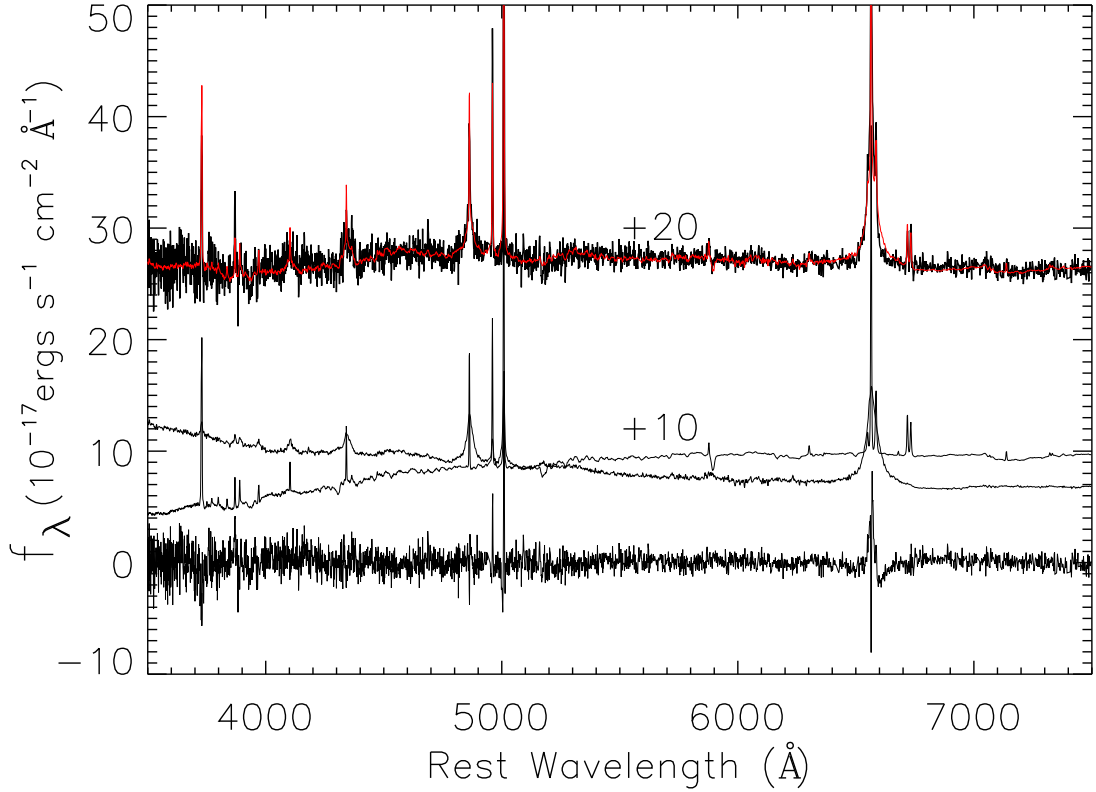


Fig. 6.— The SDSS spectrum of SDSS J094813.80+401325.9, with $z = 0.128$, a typical example of a low- S/N object in our sample, with $S/N = 15.1$. The middle components are the *reconstructed* AGN and host galaxy spectra with an offset for clarity, the top histogram is the original active galaxy spectrum with an offset for clarity, and the bottom histogram is the fit residual. The gray curve is the modeled active galaxy spectrum, which is red in the electronic version.

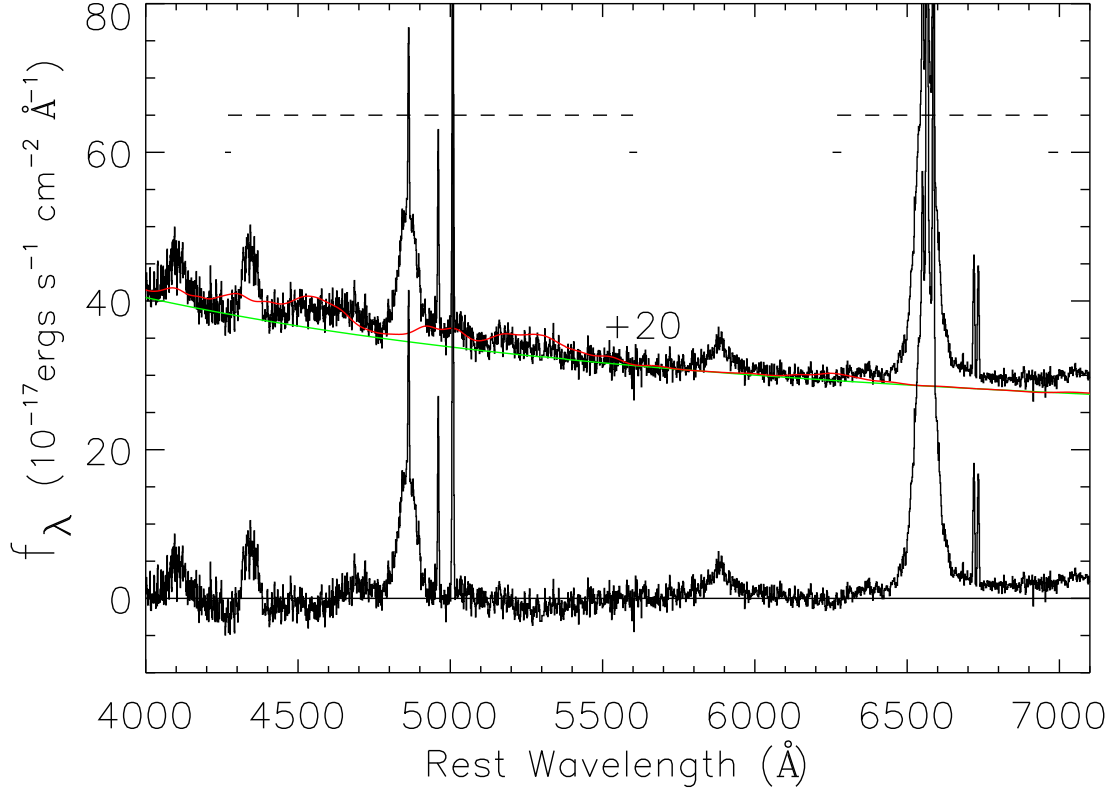


Fig. 7.— Example continuum and FeII template fit, for the object described in Figure 4. The top spectrum is the host-subtracted AGN spectrum with an offset for clarity, the middle lines are the featureless continuum and the iron template superposed on the continuum with an offset for clarity, and the bottom histogram is the AGN spectrum after subtracting the continuum and iron template. The four short horizontal solid lines denote the end points used for continuum fitting. The two horizontal dashed lines show the two continuum regions used to fit the broken power law. In the electronic version, the green curve is the modeled continuum and the red curve is the iron template superposed on the continuum.

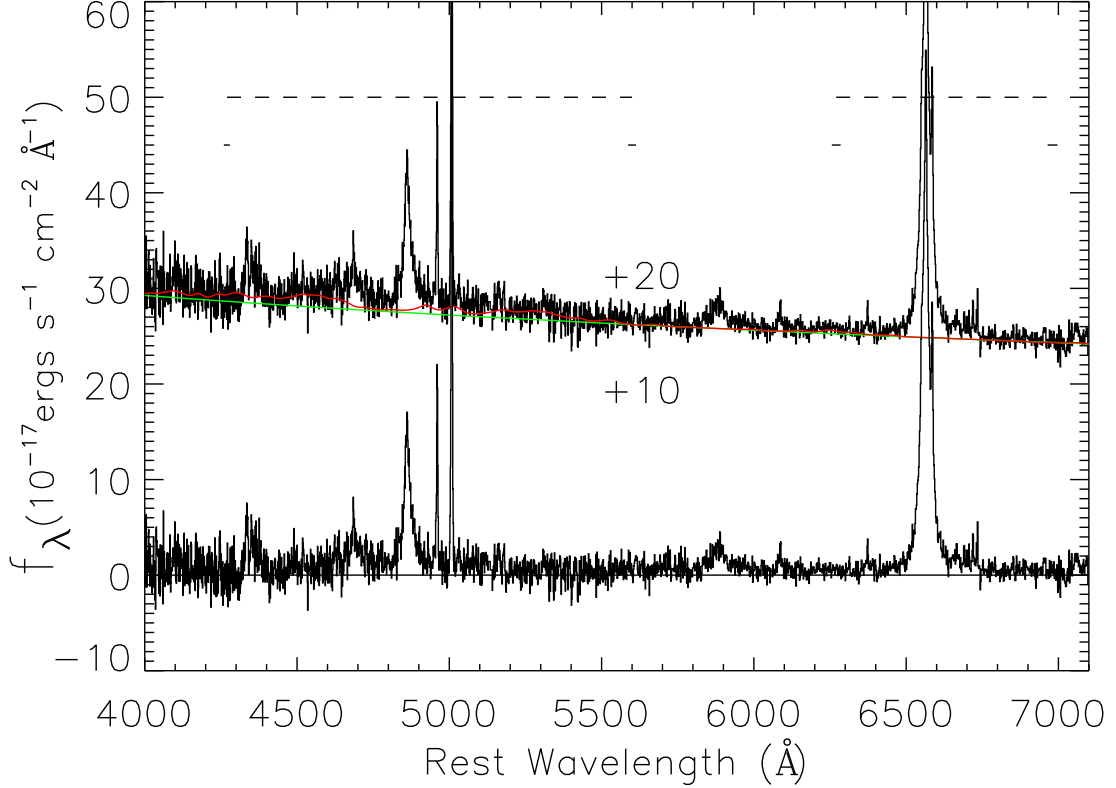


Fig. 8.— Example continuum and FeII template fit, for the object described in Figure 5. The top spectrum is the host-subtracted AGN spectrum with an offset for clarity, the middle lines are the featureless continuum and the iron template superposed on the continuum with an offset for clarity, and the bottom histogram is the AGN spectrum after subtracting the continuum and iron template. The four short horizontal solid lines denote the end points used for continuum fitting. The two horizontal dashed lines show the continuum regions used to fit the broken power law. In the electronic version, the green curve is the modeled continuum and the red curve is the iron template superposed on the continuum.

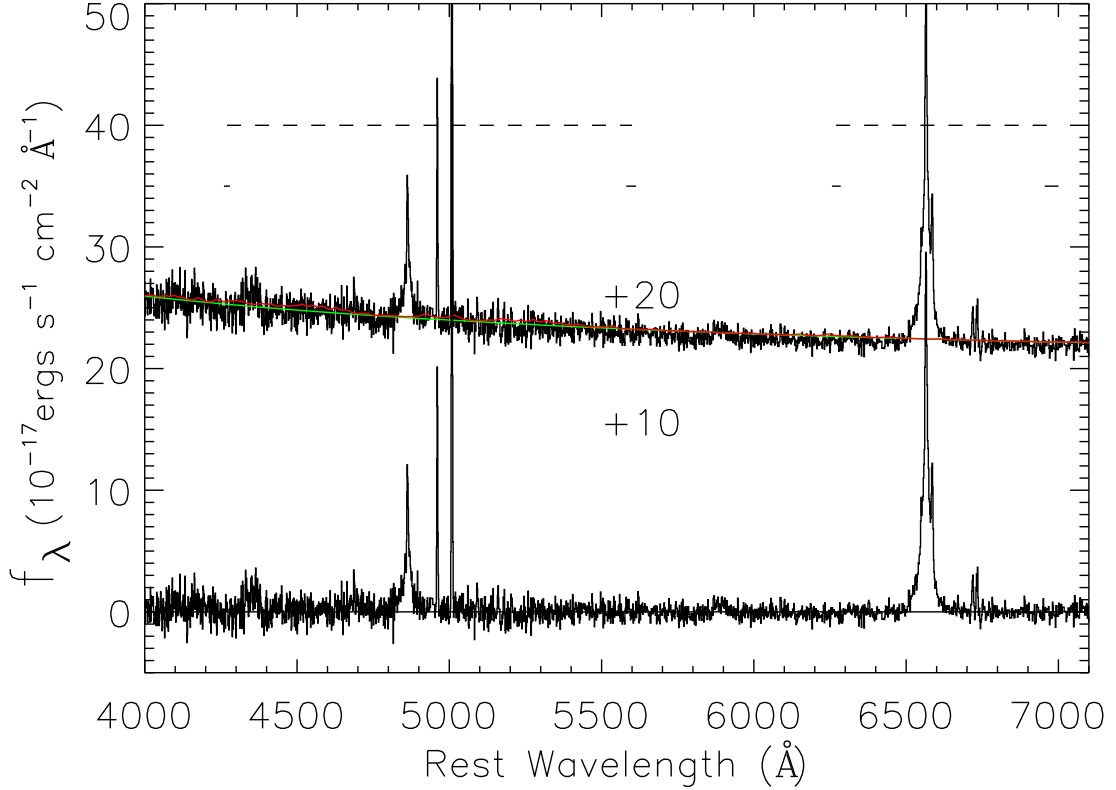


Fig. 9.— Example continuum and FeII template fit, for the object described in Figure 6. The top spectrum is the host-subtracted AGN spectrum with an offset for clarity, the middle lines are the featureless continuum and the iron template superposed on the continuum with an offset for clarity, and the bottom histogram is the AGN spectrum after subtracting the continuum and iron template. The four short horizontal solid lines denote the end points used for continuum fitting. The two horizontal dashed lines show the continuum regions used to fit the broken power law. In the electronic version, the green curve is the modeled continuum and the red curve is the iron template superposed on the continuum.

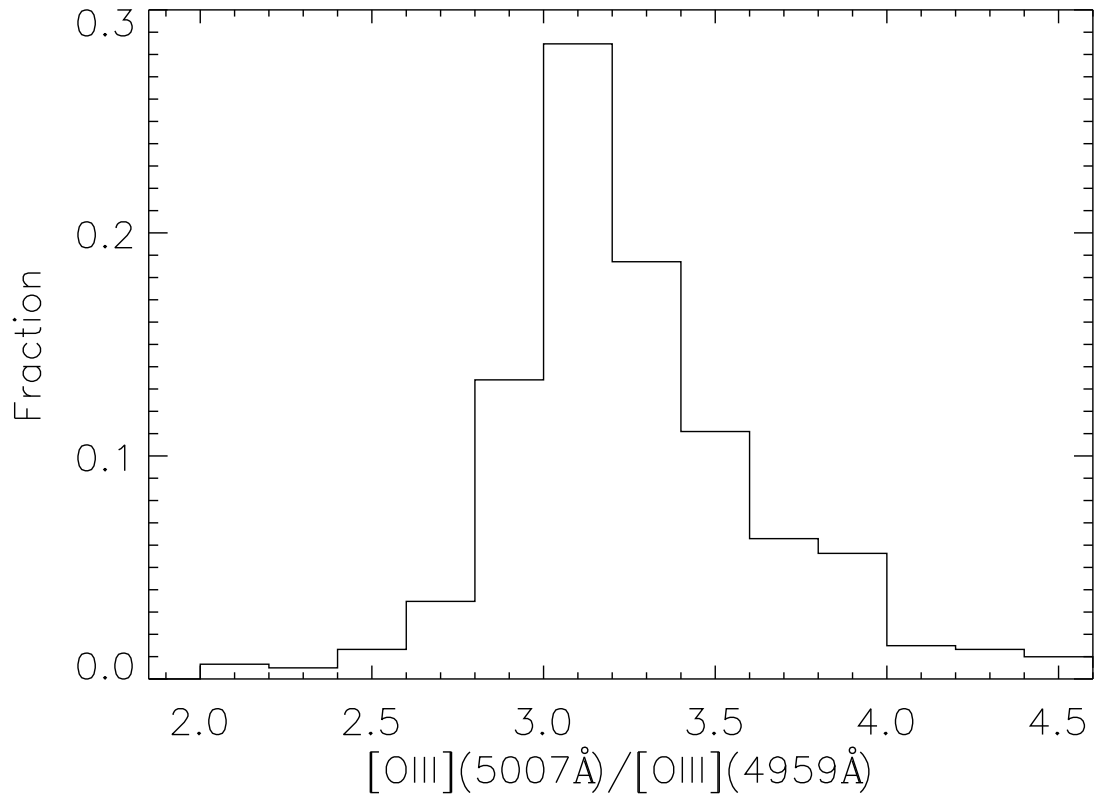


Fig. 10.— Distribution of the O III doublet flux ratio ($F(5007\text{\AA})/F(4959\text{\AA})$). The distribution shows that most O III doublet ratios are close to the theoretical value of 3:1.

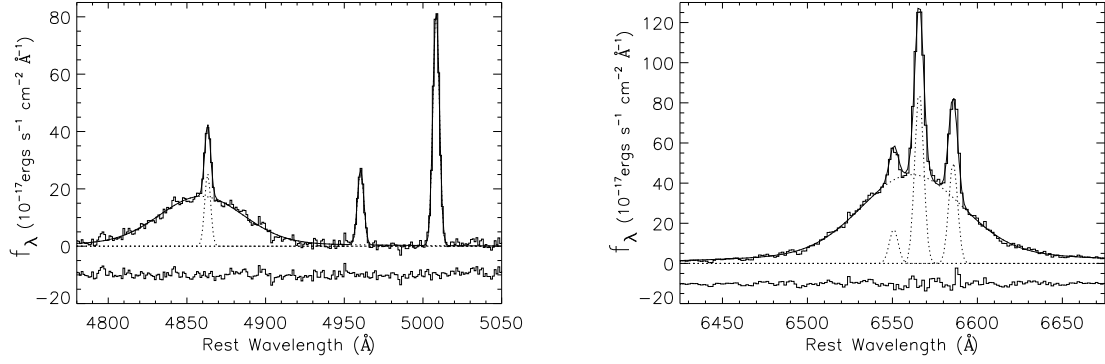


Fig. 11.— Example line fit for the object described in Figs. 4 and 7. Left panel: Fits to the $H\beta + O\ III\lambda\lambda\ 4959, 5007\text{\AA}$ region. The data are shown by the histogram, the fitted broad and narrow components are shown as dotted lines, and the sum of all components is shown as a solid line. The bottom histogram is the fit residual with an offset of -10 for clarity. Right panel: Same as the figure to the left, but for the $H\alpha + [NII]\lambda\lambda\ 6548, 6583\text{\AA}$ complex.

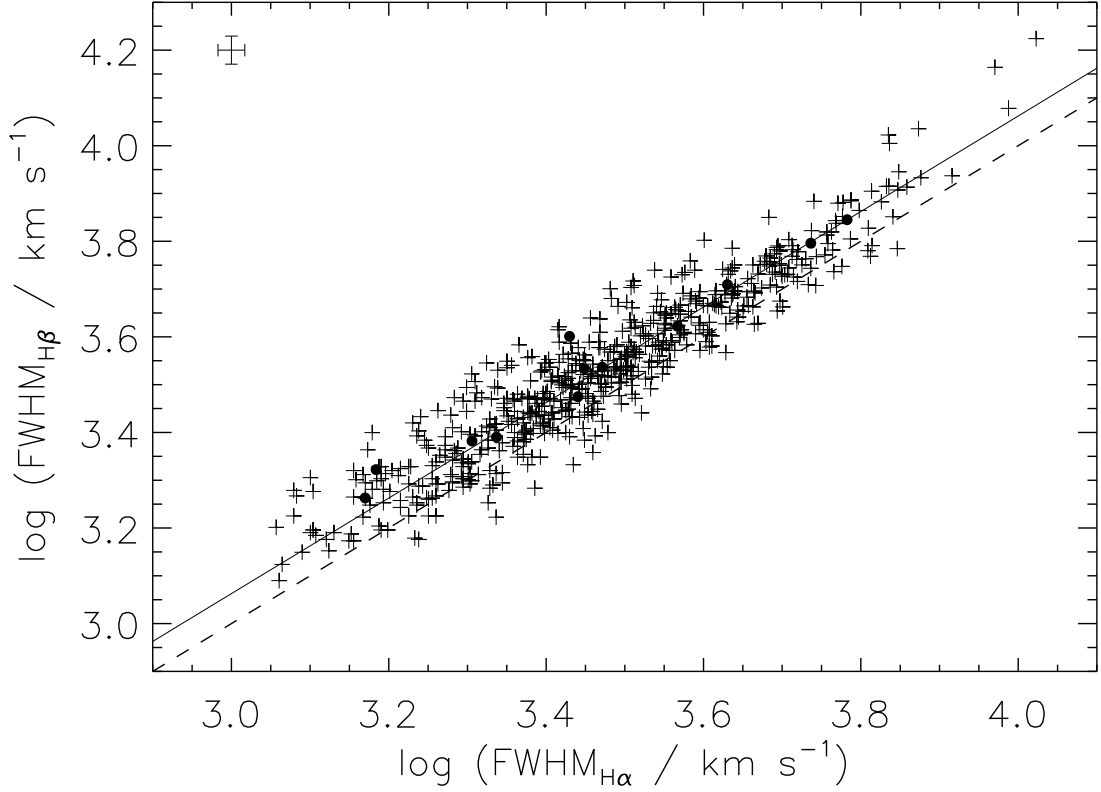


Fig. 12.— Correlation between H α and H β line widths. The solid line gives the BCES bisector fit to 597 objects. The dashed line denotes $\text{FWHM}_{\text{H}\alpha} = \text{FWHM}_{\text{H}\beta}$. The filled dots are the data from Kaspi et al. (2000), which are the mean FWHM values. A typical FWHM error bar for an individual measurement, determined by the mean of all the formal errors of FWHM measurements, is shown in the top left part of the panel.

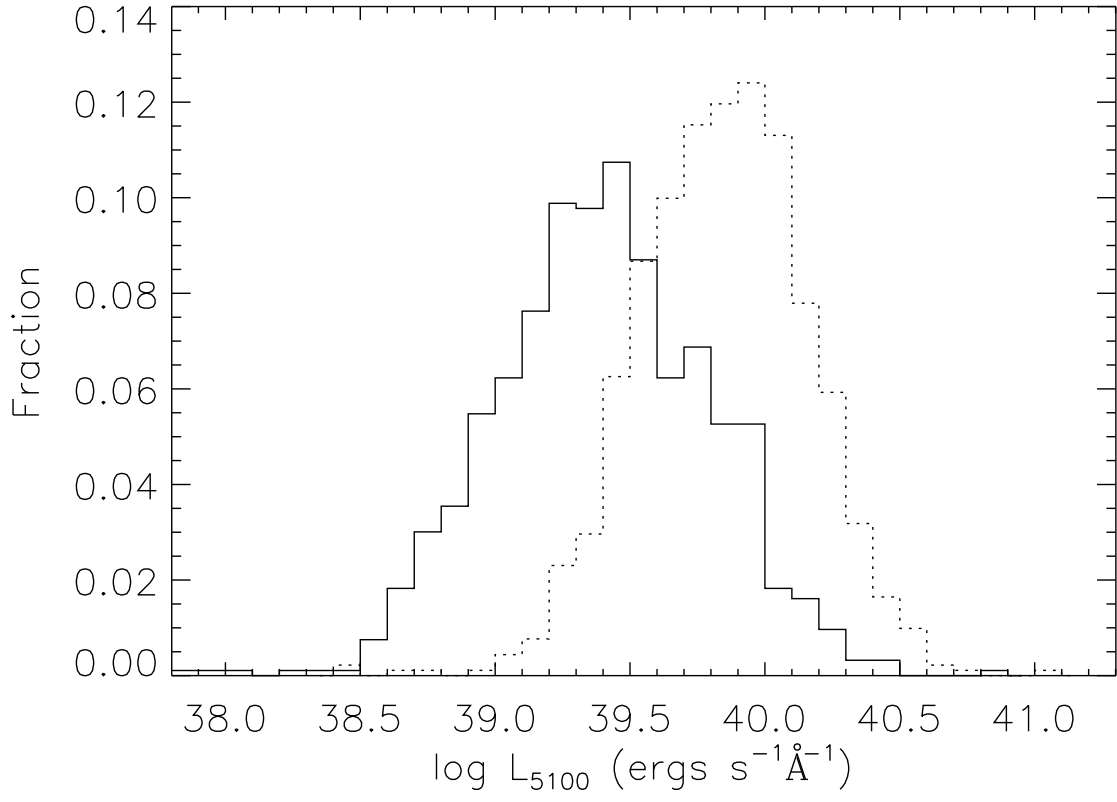


Fig. 13.— Distribution of AGN monochromatic luminosity at 5100Å, L_{5100} . The solid line shows the luminosity distribution after subtraction of the host galaxy component, and the dotted line shows the distribution without subtraction of the host galaxy.

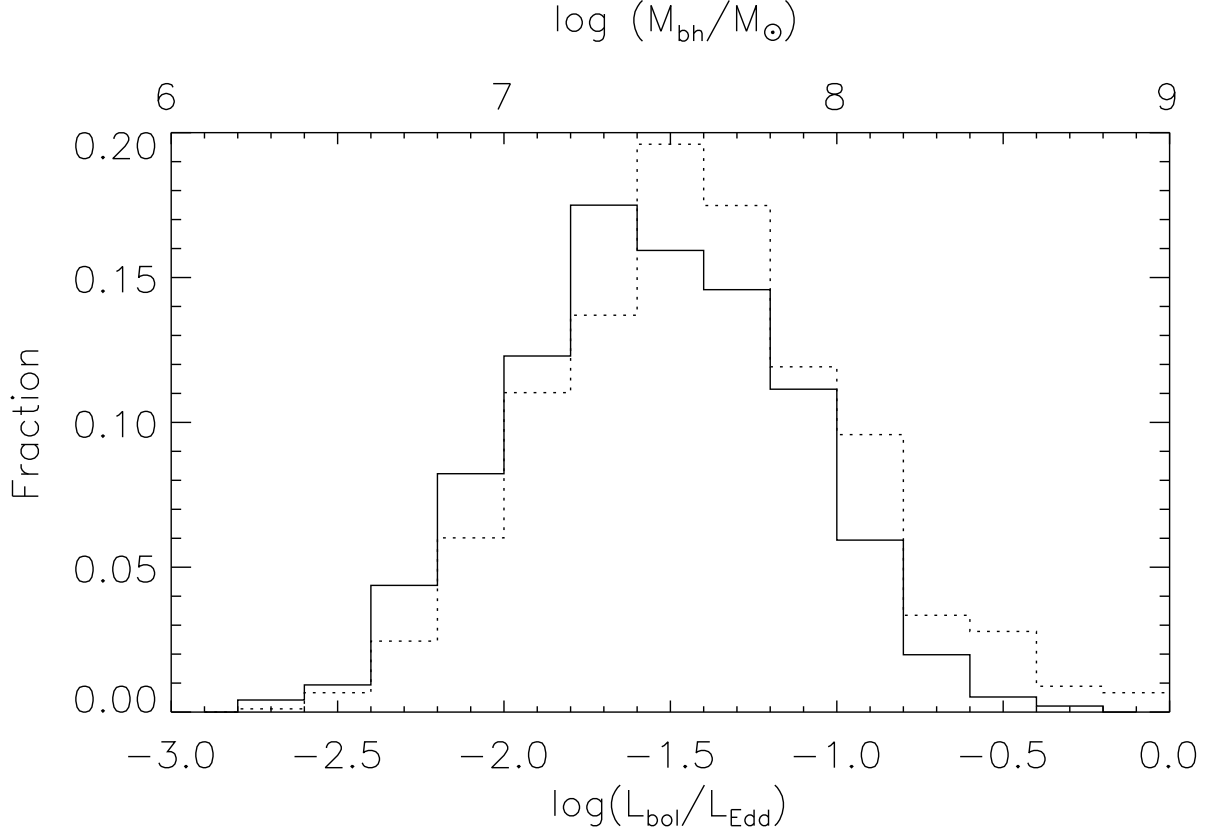


Fig. 14.— The distributions of the Eddington ratio, $\log(L_{\text{bol}}/L_{\text{Edd}})$ (solid histogram, units labeled at bottom of plot) and the BH mass, M_{BH}/M_{\odot} (dotted histogram, units labeled at top of plot). The AGN bolometric luminosity, L_{bol} , was estimated according to the approximate relation $L_{\text{bol}} \approx 10\lambda L_{\lambda}(5100\text{\AA})$.

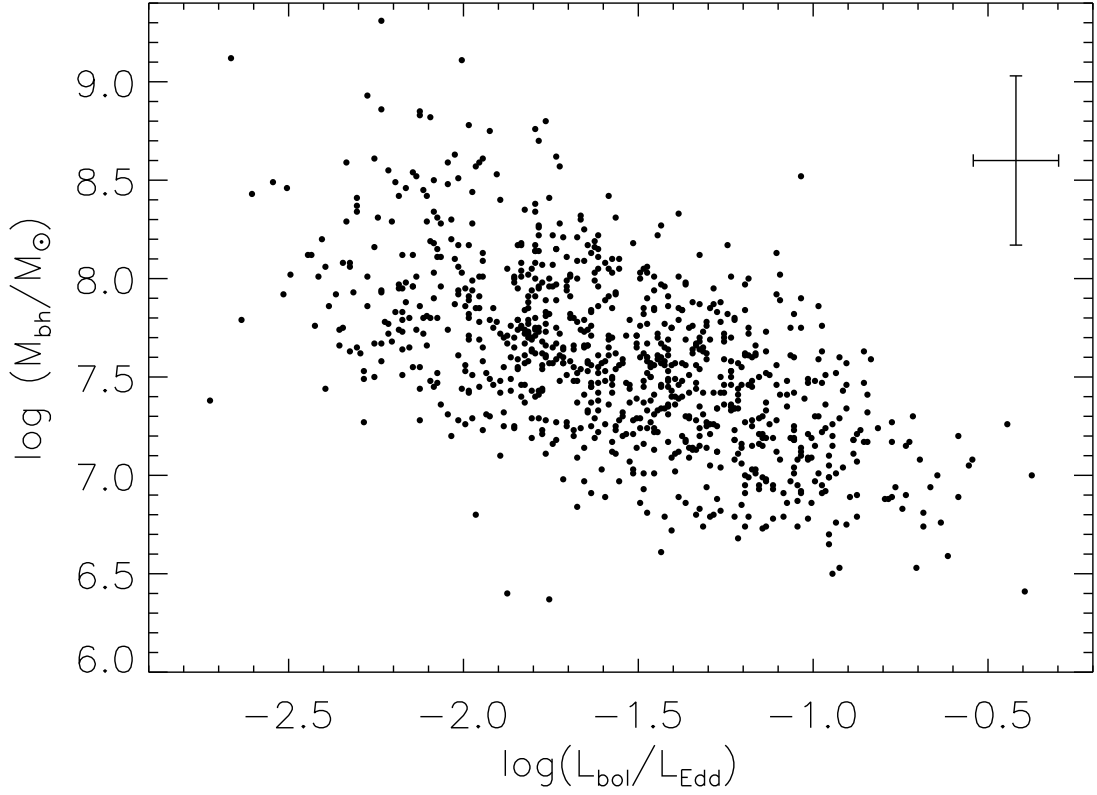


Fig. 15.— The distribution of the BH masses with the estimated Eddington ratio $L_{\text{bol}}/L_{\text{Edd}}$. The apparent anti-correlation is due to parameter interdependencies, and sample selection effects (see § 3.5). The right top horizontal line shows the typical uncertainty of the estimated Eddington ratio $L_{\text{bol}}/L_{\text{Edd}}$, due to the 25% standard deviation in the bolometric correction (Richards et al. 2006) and the BH mass estimation error. The right top vertical line shows the statistical BH masses uncertainties.

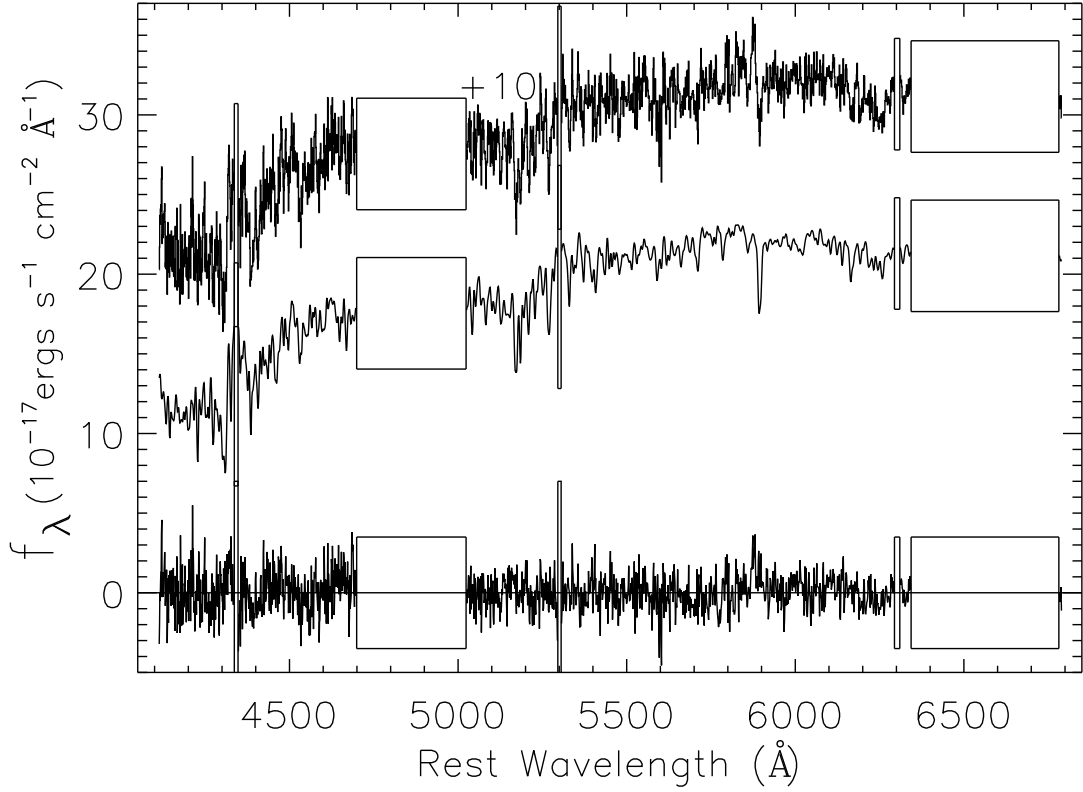


Fig. 16.— An example host galaxy fit to measure the velocity dispersion. The top line is the *decomposed* host galaxy spectrum with an offset 10 for clarity, the middle solid line is the fit, and the bottom solid line is the fit residual. The boxes show the masked regions. The two large boxes are masks for $\text{H}\beta$ and $\text{H}\alpha$, the left and right narrow boxes are masks for $\text{H}\gamma$ and $[\text{OI}]$, and the middle box is a mask for bad pixels.

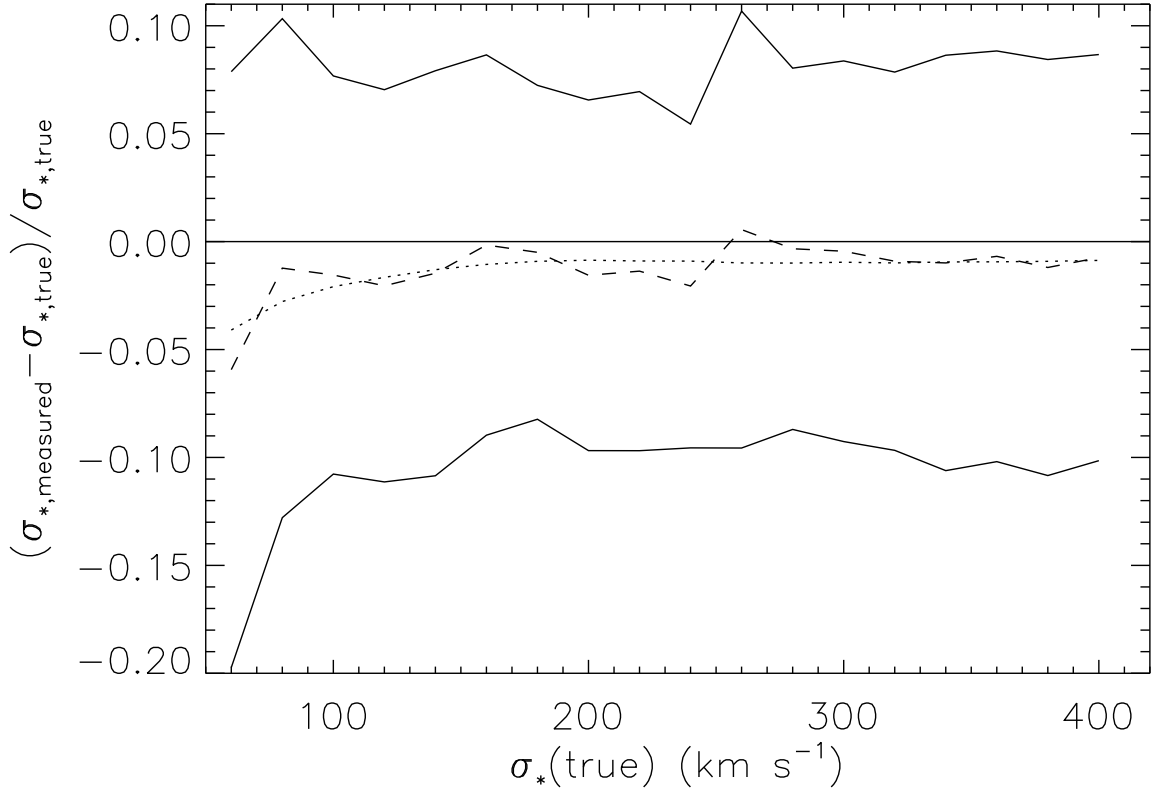


Fig. 17.— The relative systematic error and random error in the measurement of velocity dispersion, found from simulations. The dotted line shows the relative error between the true velocity and the measured noiseless velocity. The dashed line shows the relative error between the true velocity and the mean velocity in 100 simulations with noise added, for the case of spectroscopic $S/N = 15$, and host galaxy flux fraction $F_H = 50\%$. The solid curves show the standard deviations of the relative velocity measurements in 100 simulations.

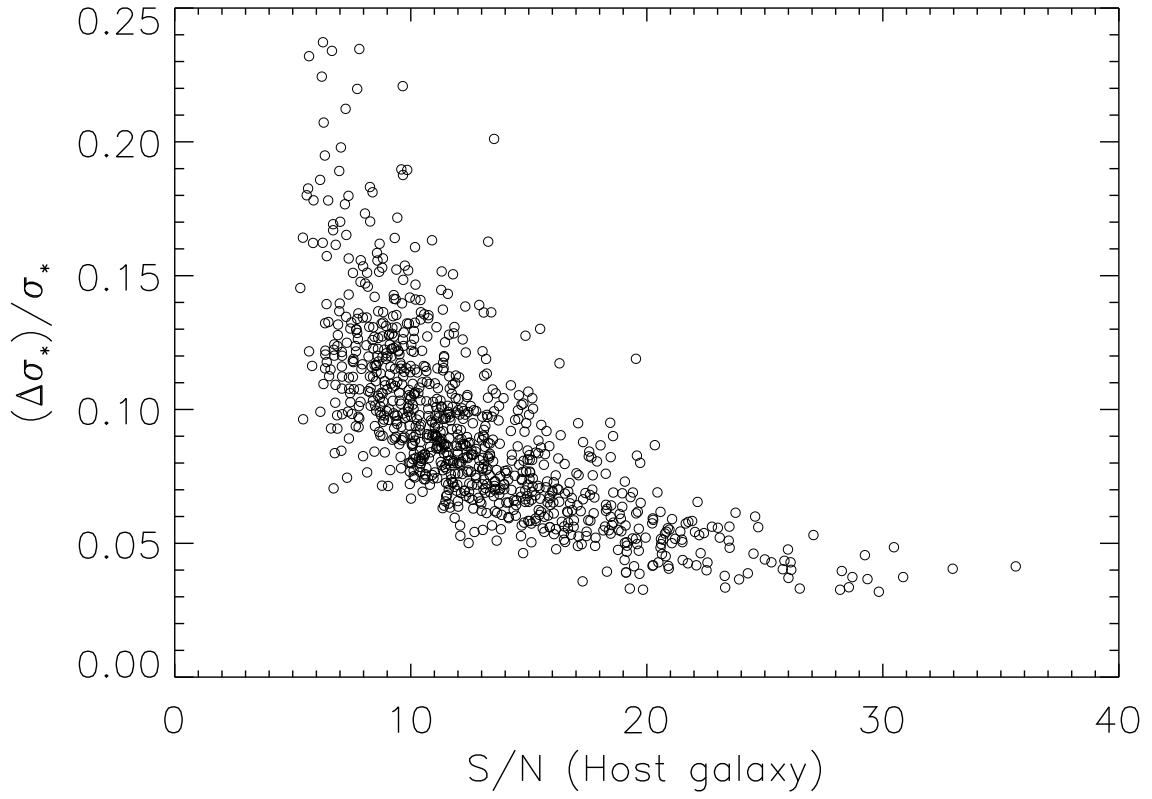


Fig. 18.— The measurement error of the velocity dispersion in the host galaxy sample, returned from the *vdisffit* routine, as a function of host galaxy spectroscopic S/N .

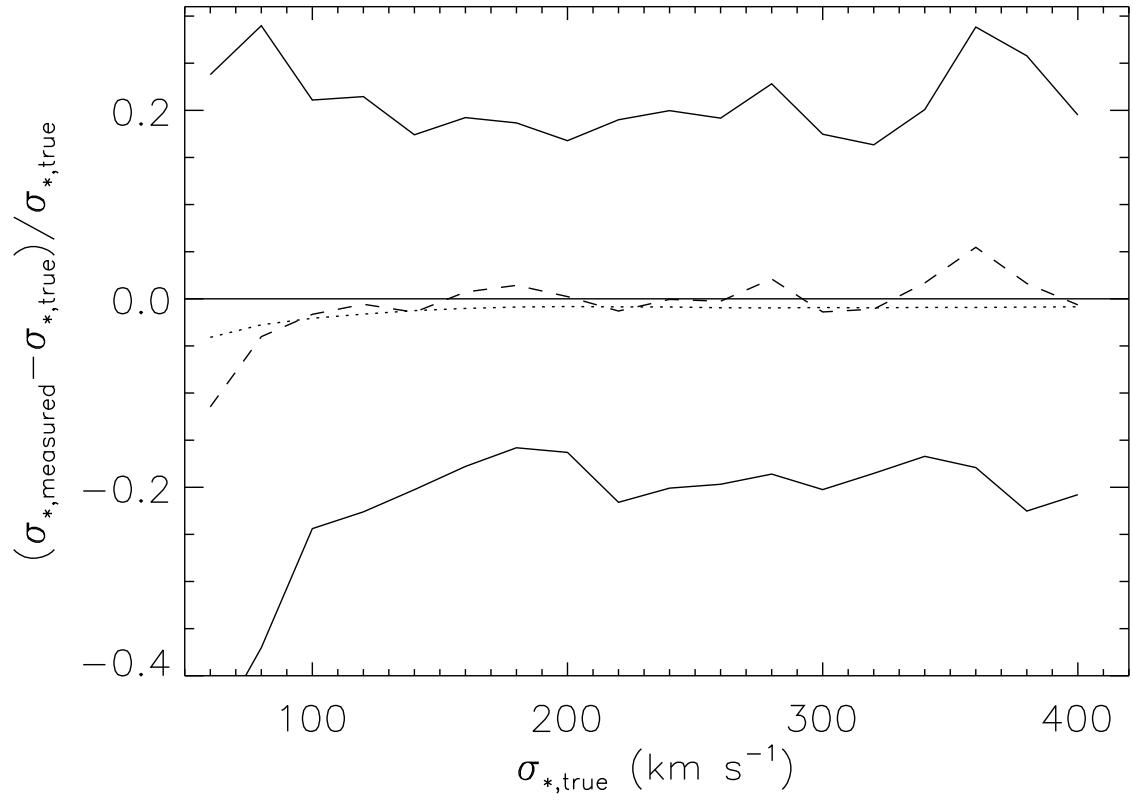


Fig. 19.— Same as Fig. 17, but for the worst case of spectroscopic $S/N = 15$, and host galaxy flux fraction $F_H = 20\%$.

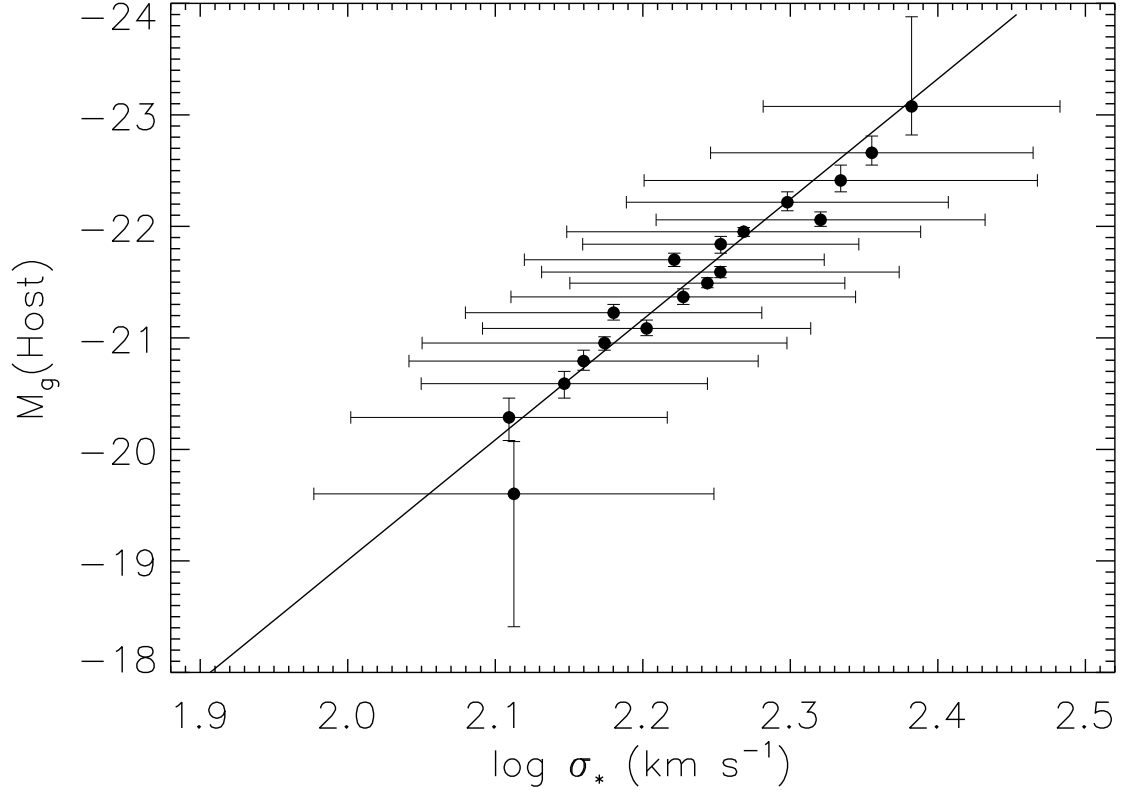


Fig. 20.— Relation between host galaxy g band absolute magnitudes M_g , and stellar velocity dispersion σ_* . Filled circles show the mean values of $\log \sigma_*$ in sets of objects that span small ranges in absolute magnitude; each set contains 50 host galaxies. Vertical error bars show the M_g bin size, and horizontal error bars show the rms scatter around the mean values of σ_* . The solid line shows the best fit linear relation (in logarithmic space).

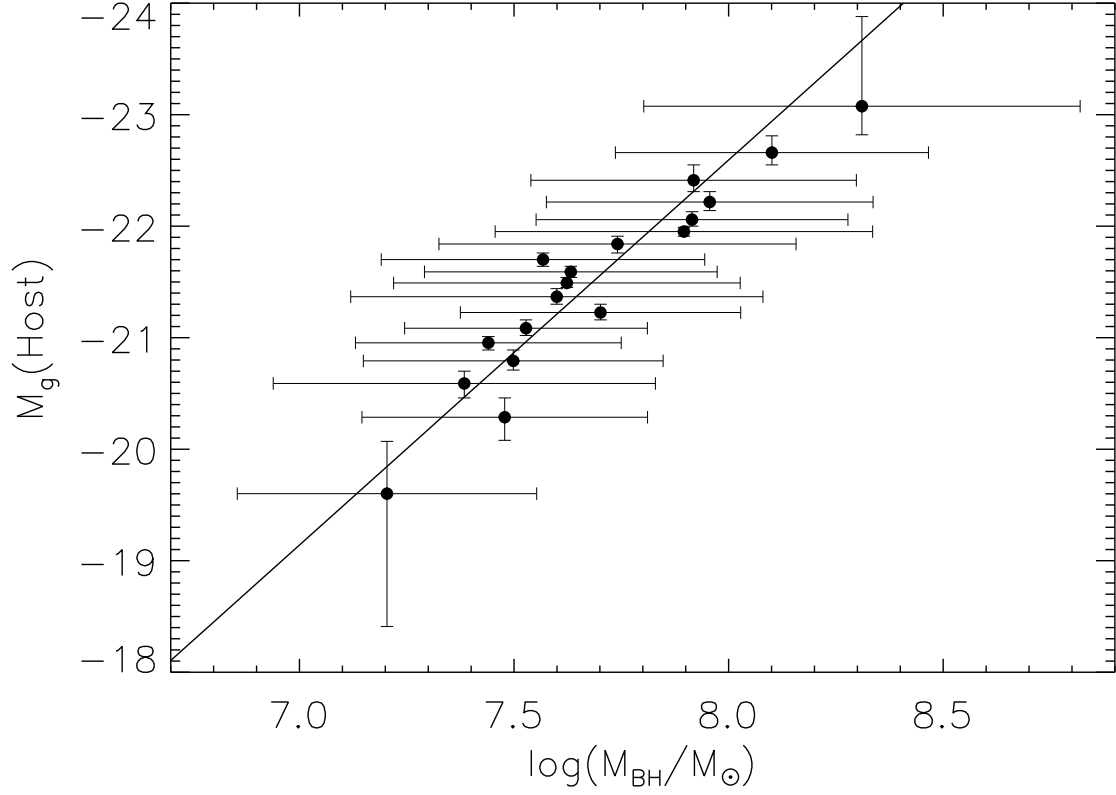


Fig. 21.— Host galaxy absolute g band magnitude vs. BH mass. The data are binned by M_g in the same way as in Fig. 20. Filled circles show the mean value of M_{BH}/M_\odot in each bin. The horizontal error bars show the rms scatter around the mean BH values, and the vertical error bars show the M_g bin size.

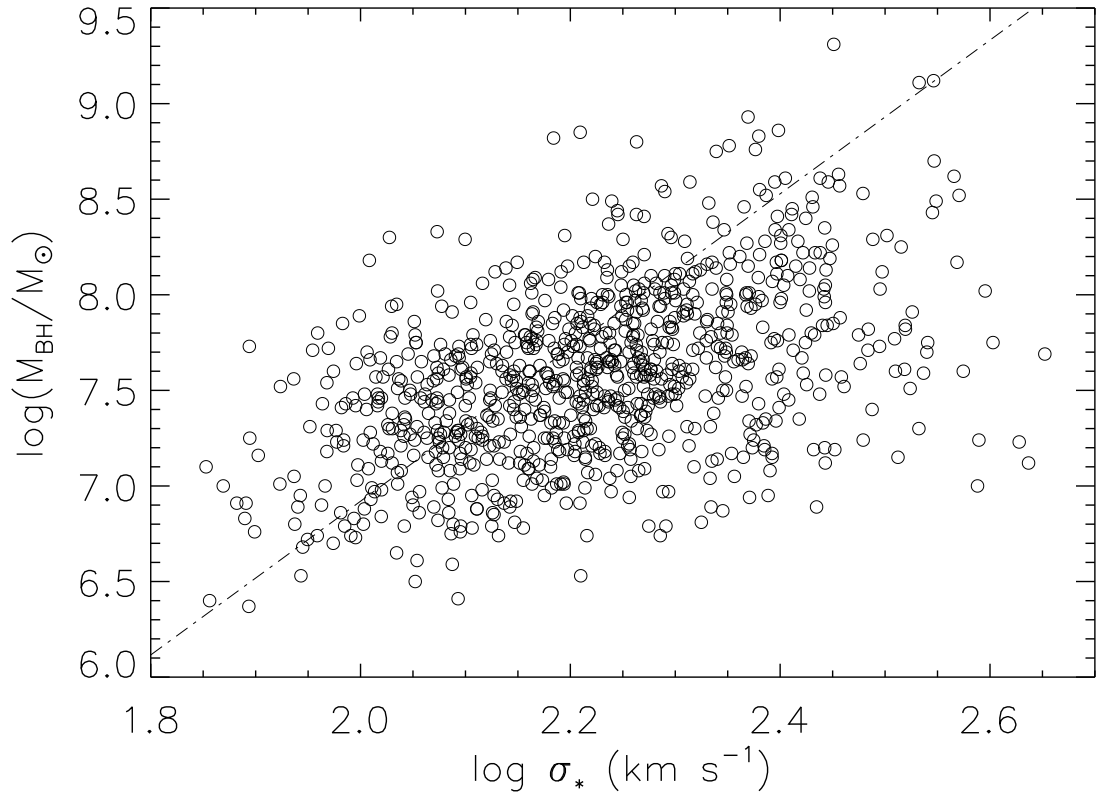


Fig. 22.— Black hole mass vs. stellar velocity dispersion for individual points. The dot-dashed line shows the best fit for inactive galaxies (Tremaine et al. 2002)

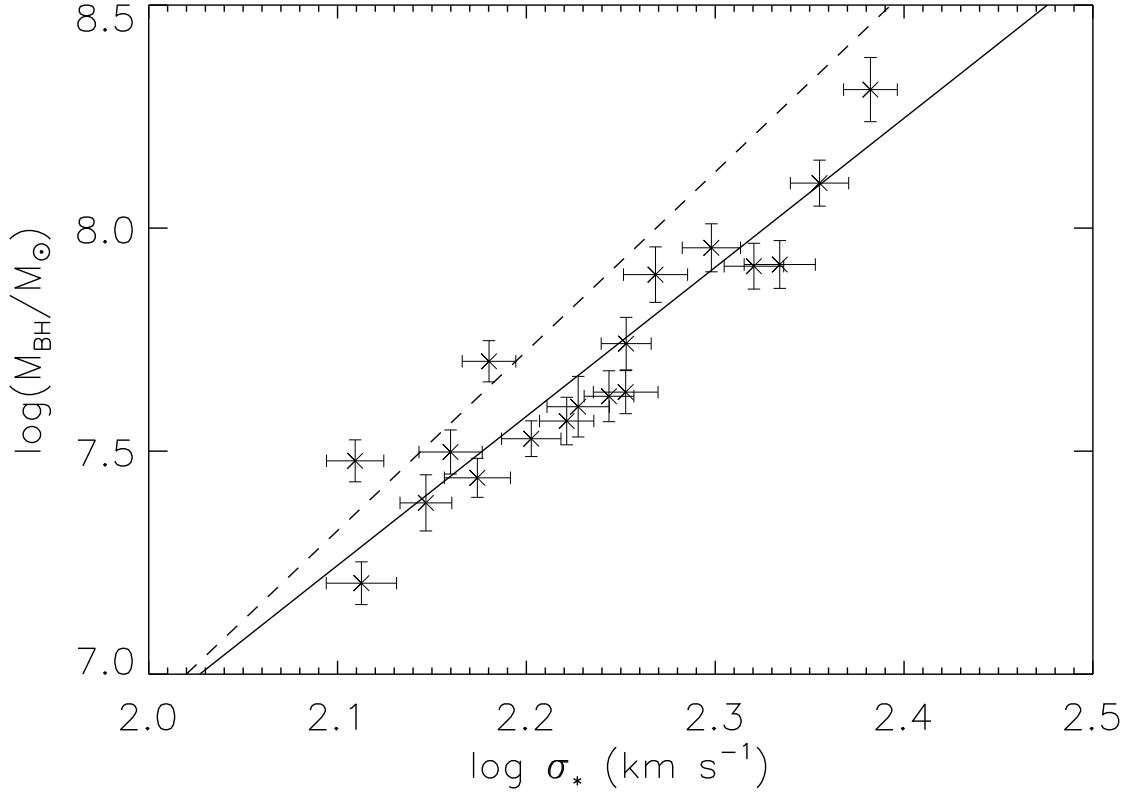


Fig. 23.— Black hole mass vs. stellar velocity dispersion in binned data. The solid line is the best-fitting linear relation (in logarithmic space), which gives the slope 3.34 ± 0.24 and intercept 7.92 ± 0.02 . The dashed line is the Tremaine et al. (2002) relation for inactive galaxies. Each point represents 50 objects which have been binned by host galaxy absolute magnitude, as in Figs. 20 and 21. The crosses show the mean value in each bin, and error bars are the standard deviation of the mean in each bin.

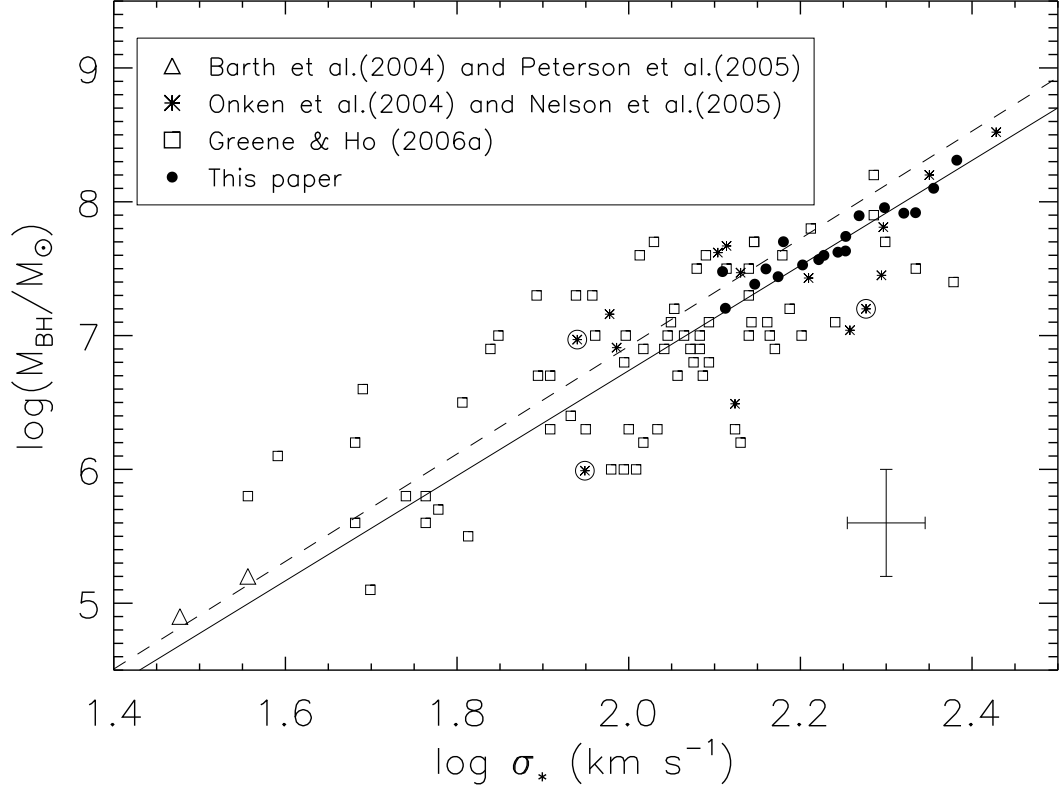


Fig. 24.— Black hole mass vs. stellar velocity dispersion for several different data sets, covering a larger dynamic range than Fig. 23. The filled circles are the data from this paper. The asterisks are the data from Onken et al. (2004) and Nelson et al. (2004), who used reverberation mapping measurements. The open squares are the data from Greene & Ho (2006a), and the open triangles are the data from Peterson et al. (2005) and Barth et al. (2004) for NGC 4395 and POX 52 respectively. The encircled objects are NLS1s. All the literature data values and their uncertainties are available in the table from Greene & Ho (2006a). The solid line is the best-fit relation for all of the data (this paper and the literature data combined). For comparison, the dashed line shows the best-fit relation for inactive galaxies, as found by Tremaine et al. (2002). Typical uncertainties in the measurements of BH mass and velocity dispersion for individual objects are shown in the bottom right corner.

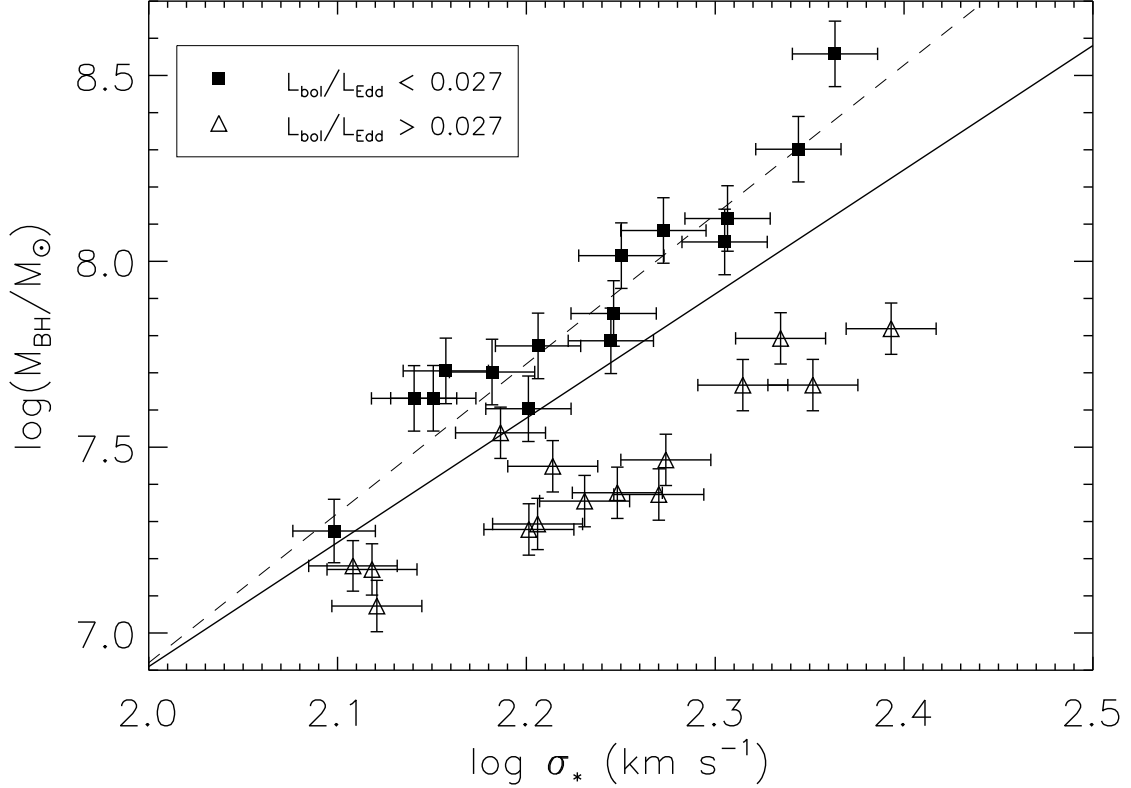


Fig. 25.— The $M_{\text{BH}} - \sigma_*$ relationship for two samples divided by the mean value of the Eddington ratio, $L_{\text{bol}}/L_{\text{Edd}}$. Mean values of M_{BH} and σ_* for objects with $L_{\text{bol}}/L_{\text{Edd}}$ below the median value of 0.027, are shown with filled squares; open triangles show the mean values for objects with $L_{\text{bol}}/L_{\text{Edd}}$ above the median value. Each sample has contributions from 451 objects, and each point represents the mean values for at least 30 objects. The error bars are the standard deviation of the mean in each bin. The solid line shows the best fit relation from equation (8). The dashed line is the Tremaine et al. (2002) relation for inactive galaxies.

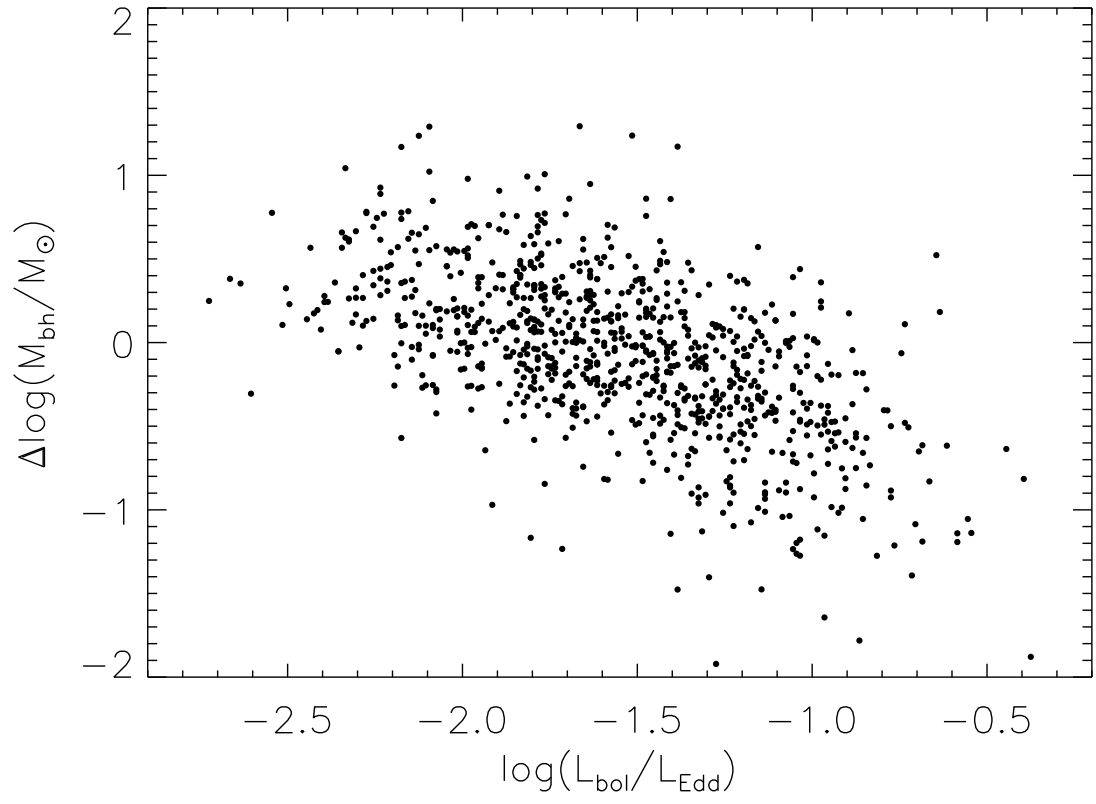


Fig. 26.— The BH mass difference between the measured BH mass and BH mass predicted by equation (8) versus the Eddington ratio, $L_{\text{bol}}/L_{\text{Edd}}$.

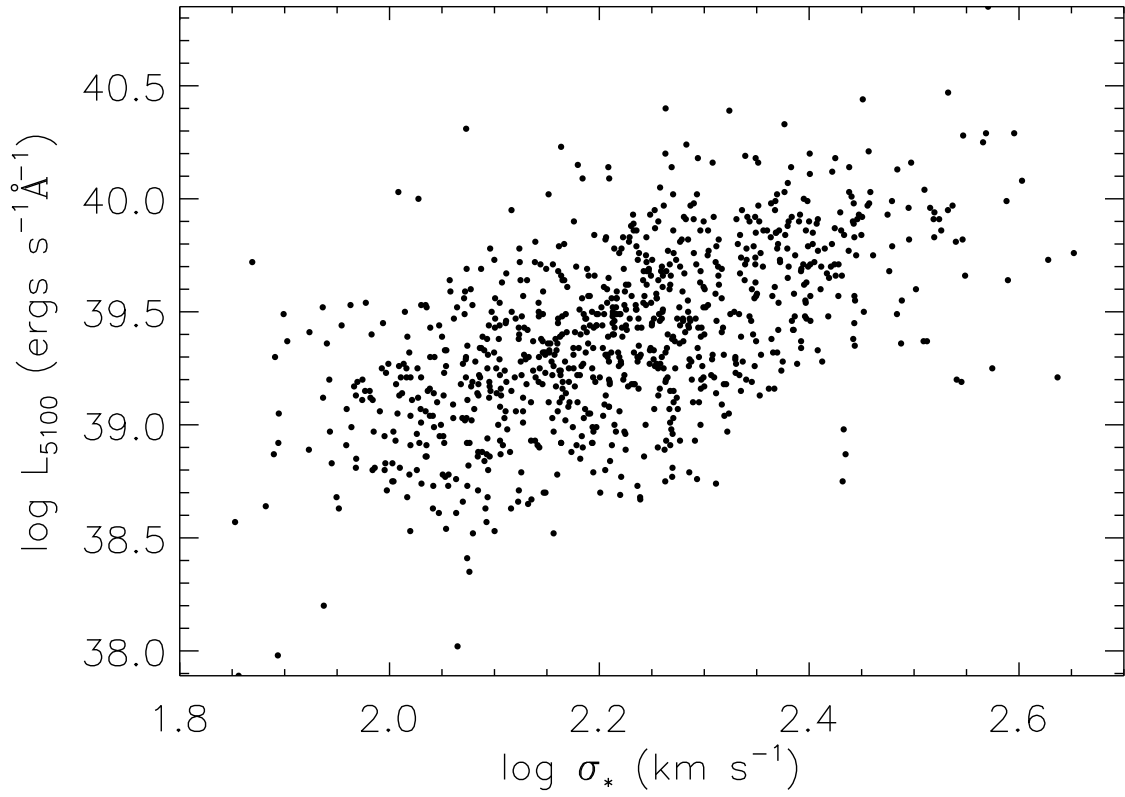


Fig. 27.— The distribution of the host galaxy velocity dispersion with the AGN monochromatic luminosity at 5100Å.

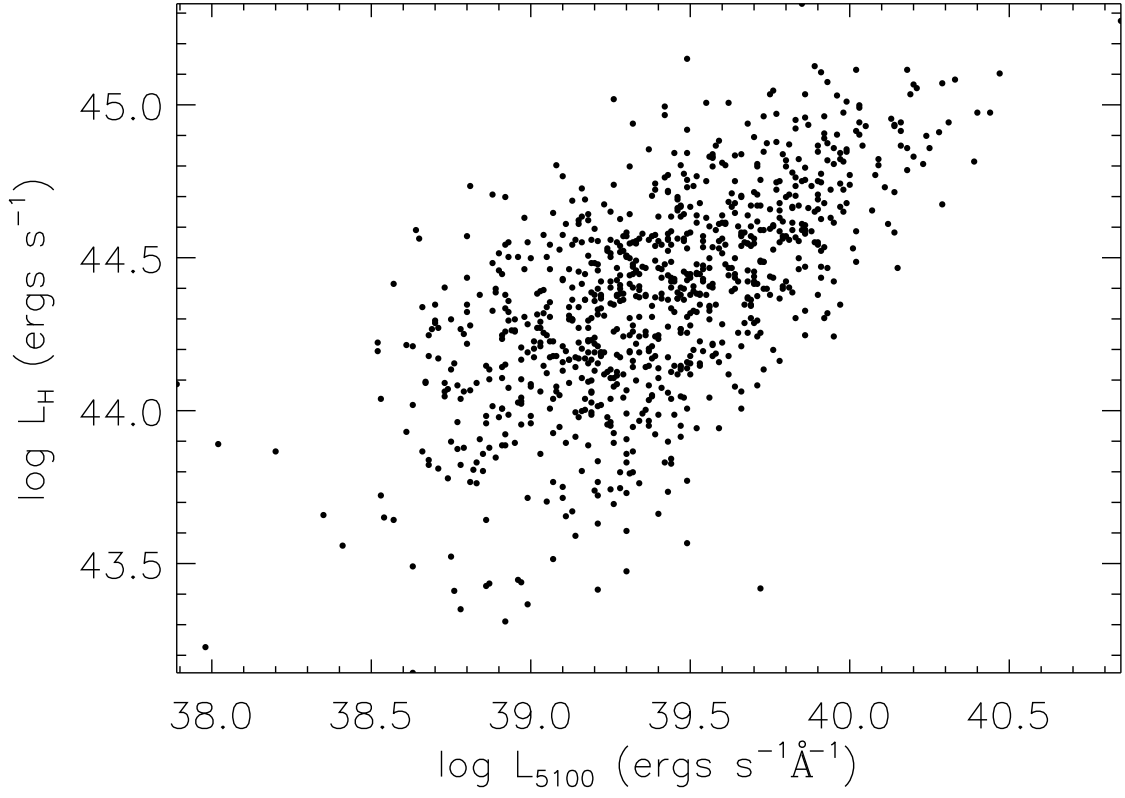


Fig. 28.— The distribution of the host galaxy g band luminosity L_H , with the AGN monochromatic luminosity at 5100Å. The apparent correlation may be due in part to sample selection effects.

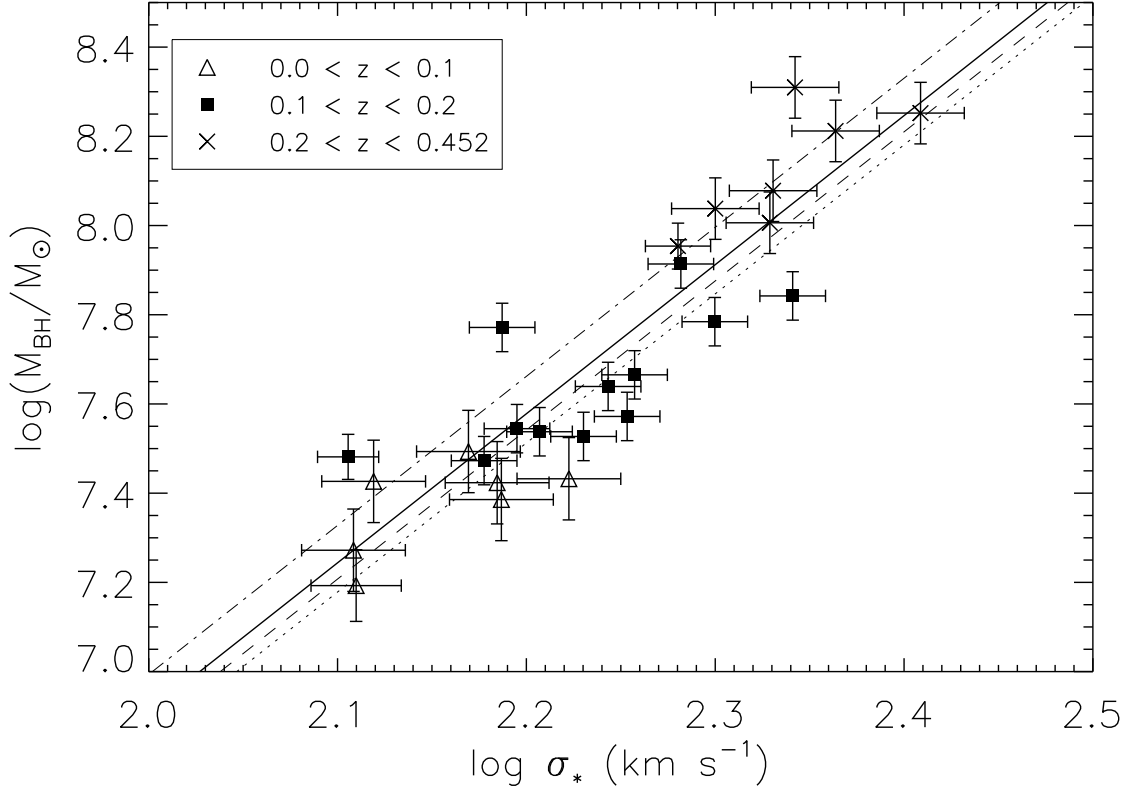


Fig. 29.— The $M_{\text{BH}} - \sigma_*$ relationship in different redshift ranges. Objects with redshifts from 0 to 0.1 are represented with open triangles, which show the weighted average values in bins containing measurements from at least 25 objects. Filled squares show the mean values for objects with redshifts from 0.1 to 0.2; each point has contributions from at least 40 objects. Crosses show the mean values for objects with redshifts from 0.2 to 0.452; each point represents data from at least 30 objects. The error bars are the standard deviation of the mean in each bin. The solid line shows the best fit relation from equation (8). With the slope fixed at the value in equation (8), the dotted, dashed and dot-dashed lines show the best fits for the three bins with redshifts from low to high respectively.

Table 1. Sample Properties

Name (1)	z (2)	m_i (3)	F_H (4)	ϕ (5)	S/N (6)	$S/N(\text{Host})$ (7)	$M_g(\text{Host})$ (8)	$\log L_{5100}(1)$ (9)	$\log L_{5100}(2)$ (10)	σ_* (11)	σ_c (12)	$\text{FWHM}_{H\beta}$ (13)	$\text{FWHM}_{H\alpha}$ (14)	$\log M_{\text{BH}}$ (15)	$L_{\text{bol}}/L_{\text{Edd}}$ (16)
000611.54+145357.2	0.1186	15.79	0.41	2.30	25.9	15.7	-22.47	39.52	39.90	181.1±13.4	188.9	3.39±0.11	3.13±0.05	6.96± 0.07	0.1568
000729.98−005428.0	0.1454	17.55	0.53	3.54	15.3	9.6	-20.71	39.08	39.65	121.2±17.8	127.5	3.30±0.32	2.92±0.07	6.63± 0.19	0.1217
000805.62+145023.3	0.0455	14.93	0.65	3.70	44.9	29.2	-20.78	38.67	39.37	173.1± 7.9	173.4	6.09±0.25	7.02±0.07	6.88± 0.09	0.0266
000813.22−005753.3	0.1393	16.45	0.46	3.64	27.5	13.3	-21.75	39.61	39.97	221.8±17.6	232.9	5.21±0.24	3.24±0.05	7.39± 0.10	0.0717

Note. — Col.(1):Name (SDSS J). Col.(2): Redshift. Col.(3): i band magnitude. Col.(4): Host galaxy fraction. Col.(5): Galaxy classification angle (degrees). Col.(6): i band spectroscopic S/N . Col.(7): Host galaxy S/N . Col.(8): Host galaxy absolute g band magnitude. Col.(9): L_{5100} ($\text{ergs s}^{-1}\text{\AA}^{-1}$, host subtracted). Col.(10): L_{5100} ($\text{ergs s}^{-1}\text{\AA}^{-1}$, host not subtracted). Col.(11): Host galaxy velocity dispersion (km s^{-1}), uncorrected for finite fiber diameter. Col.(12): Host galaxy velocity dispersion (km s^{-1}), corrected for finite fiber diameter by equation (4). Col.(13): $\text{FWHM}_{H\beta}$ (10^3km s^{-1}). Col.(14): $\text{FWHM}_{H\alpha}$ (10^3km s^{-1}). See §3.2 for the error estimates of $\text{FWHM}_{H\alpha}$ and $\text{FWHM}_{H\beta}$. Col.(15): M_{BH} (M_{\odot}), calculated from equation (2) by $\text{FWHM}_{H\beta}$. The symbol '*' indicated where $\text{FWHM}_{H\beta}$ was obtained from $\text{FWHM}_{H\alpha}$ by equation (3). The M_{BH} uncertainties are formal uncertainties, actual uncertainties are probably dominated by systematics in BLR geometry. Col.(16): $L_{\text{bol}}/L_{\text{Edd}}$. From Col.(13) to Col.(16), some quantities are set to zeros. These default values are given for entries with bad spectra or measurements (see §3.3). Table 1 is available in the electronic edition. A portion is shown here for guidance regarding its form and content.

Table 2. Mean properties in host galaxy luminosity bins

$M_g(\text{H})$ (1)	$M_{g,faint}(\text{H})$ (2)	$M_{g,bright}(\text{H})$ (3)	$\log M_{\text{BH}}$ (4)	$\Delta \log M_{\text{BH}}$ (5)	$\log \sigma_*$ (6)	$\Delta \log \sigma_*$ (7)
-23.08	-22.82	-23.88	8.31	0.51	2.38	0.10
-22.66	-22.55	-22.81	8.10	0.36	2.36	0.11
-22.41	-22.31	-22.55	7.92	0.38	2.33	0.13
-22.22	-22.14	-22.31	7.96	0.38	2.30	0.11
-22.06	-22.00	-22.13	7.91	0.36	2.32	0.11
-21.95	-21.91	-21.99	7.90	0.44	2.27	0.12
-21.84	-21.76	-21.91	7.74	0.42	2.25	0.09
-21.70	-21.64	-21.76	7.57	0.38	2.22	0.10
-21.59	-21.54	-21.64	7.63	0.34	2.25	0.12
-21.49	-21.45	-21.54	7.62	0.40	2.24	0.09
-21.37	-21.30	-21.44	7.60	0.48	2.23	0.12
-21.23	-21.16	-21.30	7.70	0.33	2.18	0.10
-21.08	-21.02	-21.16	7.53	0.28	2.20	0.11
-20.95	-20.89	-21.01	7.44	0.31	2.17	0.12
-20.79	-20.71	-20.89	7.50	0.35	2.16	0.12
-20.59	-20.46	-20.70	7.38	0.45	2.15	0.10
-20.29	-20.08	-20.46	7.48	0.33	2.11	0.11
-19.60	-18.41	-20.07	7.20	0.35	2.11	0.14

Note. — 903 objects with reliable parameter measurements were dividend into 18 bins; each bin contains 50 objects except the last bin which contains 53 objects. Col.(1): Mean host galaxy g band absolute magnitude in the bin. Col.(2): Faintest host galaxy g band absolute magnitude in the bin. Col.(3): Brightest host galaxy g band absolute magnitude in the bin. Col.(4): The weighted mean of the $\log M_{\text{BH}}(M_{\odot})$ in the bin. Col.(5): The dispersion of $\log M_{\text{BH}}(M_{\odot})$ in the bin. Col.(6): The weighted mean of velocity dispersion $\log \sigma_*$ in the bin. Col.(7): The dispersion of $\log \sigma_*$ in the bin.

Table 3. Partial correlation analysis for the dependence of ΔM_{BH} on Eddington ratio

x (1)	$r_{L_{\text{bol}}/L_{\text{Edd}},x}$ (2)	$r_{\Delta M,x}$ (3)	$r_{\Delta M,L_{\text{bol}}/L_{\text{Edd}};x}$ (4)	P (5)
L_{5100}	0.377	-0.081	-0.591	$< 0.01\%$
FWHM	-0.882	0.577	-0.176	$< 0.01\%$
σ_*	0.023	-0.563	-0.682	$< 0.01\%$
L_H	0.030	-0.044	-0.576	$< 0.01\%$
z	0.137	0.005	-0.583	$< 0.01\%$

Note. — Partial correlation coefficients for ΔM_{BH} with Eddington ratio. Col.(1): The control parameters in the partial correlation test. Col.(2): The correlation between Eddington ratio and the control parameter. Col.(3): The correlation between ΔM_{BH} and the control parameter. Col.(4): The partial correlation coefficient for the inverse correlation of ΔM_{BH} with Eddington ratio when the influence of the control parameter is accounted for. Col.(5): The significance of the partial correlation.

Table 4. Partial correlation analysis for the dependence of L_{5100} on σ_*

x (1)	$r_{L_{5100},x}$ (2)	$r_{\sigma_*,x}$ (3)	$r_{L_{5100},\sigma_*;x}$ (4)	P (5)
L_H	0.634	0.533	0.354	$< 0.01\%$
z	0.802	0.524	0.292	$< 0.01\%$
All ^a	–	–	0.262	$< 0.01\%$

Note. — Partial correlation coefficients for ΔM_{BH} with Eddington ratio. Col.(1): The control parameters in the partial correlation test. Col.(2): The correlation between L_{5100} and the control parameter. Col.(3): The correlation between σ_* and the control parameter. Col.(4): The partial correlation coefficient for the control parameter. Col.(5): The significance of the partial correlation.

^aSecond-order partial correlation test, accounting for both control parameters.

Table 5. Partial correlation analysis for the dependence of ΔM_{BH} on redshift

x	$r_{z,x}$	$r_{\Delta M,x}$	$r_{\Delta M,z;x}$	P
(1)	(2)	(3)	(4)	(5)
L_{5100}	0.802	-0.081	0.118	$< 0.04\%$
FWHM	0.257	0.577	-0.181	$< 0.01\%$
σ_*	0.524	-0.563	0.428	$< 0.01\%$
L_H	0.707	-0.044	0.052	11.8%
$L_{\text{bol}}/L_{\text{Edd}}$	0.142	-0.576	0.108	0.11%
All ^a	—	—	0.059	7.64%

Note. — Partial correlation coefficients for ΔM_{BH} with redshift. Col.(1): The control parameters in the partial correlation test. Col.(2): The correlation between redshift and the control parameter. Col.(3): The correlation between ΔM_{BH} and the control parameter. Col.(4): The partial correlation coefficient for the control parameter. Col.(5): The significance of the partial correlation.

^aFifth-order partial correlation test, accounting for all 5 control parameters .

